Detailed 3D structures of the western edge of the Pacific Large Low Velocity Province

Jiewen Li[1*], Baolong Zhang[2], Daoyuan Sun[3], Dongdong Tian[1] and Jiayuan Yao[1]

[1] Hubei Subsurface Multi-scale Imaging Key Laboratory, School of Geophysics and Geomatics, China University of Geosciences, Wuhan 430074, China

[2] State Key Laboratory of Geodesy and Earth's Dynamics, Innovation Academy for Precision Measurement Science and Technology, CAS, Wuhan, 430077, China

[3] Laboratory of Seismology and Physics of Earth's Interior, School of Earth and Space Sciences, University of Science and Technology of China, Hefei, Anhui, China

Corresponding author: *Jiewen Li (lijiewen@cug.edu.cn)

Key Points:

- Complex structures are present at the western edge of the Pacific LLVP
- Drastically varied waveforms in azimuth suggest a sharp transitional boundary among the complex structures
- The 3D structures of the western edge of the Pacific LLVP are strongly influenced by the subducted slab

Abstract

Large Low Velocity Provinces (LLVPs) are situated oppositely in the lowermost mantle beneath the Pacific Ocean and Africa. Deciphering the detailed seismic structures at the edge of LLVPs can provide key information on the composition and dynamics in the deep Earth. Here, we provide a detailed seismic image at the western edge of the Pacific LLVP by dense recordings. Differential travel time residuals and amplitude ratios between ScS and S outline the S-wave western boundary of the Pacific LLVP, suggesting the complex structures including low/high-velocity patches in the lowermost mantle in our study region. We determine the 3D low-velocity structure by modeling the delayed ScS and high-velocity D″ layer structure by modeling the anomalous Scd, with tight constraints from multiple events data. The drastically varied waveforms in azimuth suggests a sharp transitional boundary among the complex structures. After comparing the velocity structures in adjacent regions, we propose that the 3D structures of the western edge of the Pacific LLVP are strongly influenced by the vigorous mantle flow associated with the actively subducted slab.

Plain Language

Seismic studies reveal two large-scale low-velocity anomalies in the lowermost mantle beneath the Pacific Ocean and Africa, respectively. Resolving the detailed structures at their edges is crucial for understanding the geodynamic evolution in the deep Earth. In this study, we determine the location of the western boundary of the Pacific anomaly by the measured travel time and amplitude of seismic waves that across through our study region. Dense recordings show that there are complex structures at the western edge of the Pacific anomaly, and we determine the 3D structures by modeling the seismic recordings. We conclude that the 3D structures of the western edge of the Pacific anomaly are majorly influenced by the actively subducted materials after comparing the greatly different structures in adjacent regions.

1 Introduction

Global tomographic models reveal two Large Low Velocity Provinces (LLVPs) situated in the lowermost mantle beneath the Pacific Ocean and Africa, respectively (French and Romanowicz, 2015; Grand, 2002; Houser et al., 2008; Lei et al., 2020; Lu et al., 2019; Ritsema et al., 2011; Simmons et al., 2010; Simmons et al., 2012). The S-wave velocity perturbations (δV_S) in the LLVPs with respect to the ambient mantle vary from -1 to -5% (He and Wen, 2009, 2012; He et al., 2006; Ni et al., 2005; Ni et al., 2002; Wen, 2001) while P-wave velocity perturbations (δV_P) from -1 to -3% (Frost and Rost, 2014; Houser et al., 2008; Koelemeijer et al., 2016), but the density variations in the LLVPs are difficult to be resolved (Ishii and Tromp, 1999, 2001, 2004; Koelemeijer et al., 2017; Lau et al., 2017; Romanowicz, 2001). The anti-correlation of δV_S and bulk sound velocity, as well as the sharp boundaries between the LLVPs and the ambient mantle suggest that the compositions of the LLVPs are more likely to be different from that of the ambient mantle (Frost and Rost, 2014; He et al., 2006; Ni et al., 2002; Sun et al., 2007; Wang and Wen, 2004), although a pure thermal origin of the LLVPs cannot be totally ruled out (Davies et al., 2012; Schuberth et al., 2009). Moreover, the geochemical isotope studies requiring untapped reservoirs for LLVPs support a primordial origin of the LLVPs (Boyet and Carlson, 2005; Carlson and Boyet, 2006).

Tomographic models also demonstrate that LLVPs are bounded by high-velocity anomalies (e.g., the circum-Pacific), which are believed to be debris of the ancient subducted slabs (Garnero and Helmberger, 1995; Richards and Engebretson, 1992). The transition from bridgmanite to post-bridgmanite under lower mantle conditions is suggested to be sensitive to temperature, preferentially occurring in relatively cold conditions, such as regions related to subduction (Murakami et al., 2004; Oganov and Ono, 2004). The sharp seismic velocity increase with depth resulting from the transition from bridgmanite to post-bridgmanite has been suggested as the source of the D″ discontinuity within ~ 300 km above the core-mantle boundary (CMB) (Murakami et al., 2004; Oganov and Ono, 2004). The triplication phase Scd generates when S-wave encounters with this high-velocity D″ layer (He and Wen, 2012; He et al., 2006; Ko et al., 2017; Li et al., 2021; Sun et al., 2016; Thomas et al., 2004).

By taking past subduction history into account, geodynamic simulation reproduces the quasi-circular shape for the Pacific LLVP and elongated shape for the African LLVP, respectively, as seen in the lower mantle tomographic models (McNamara and Zhong, 2005). More importantly, the mantle flows associated with the subducted slab in the lower mantle could shape the LLVPs significantly, particularly resulting in edges with various slope of the LLVPs and seismic velocity gradient (i.e. sharpness) between the LLVPs and the ambient mantle. Seismic images have also shown complex structures at the edge of LLVPs. For example, the Pacific LLVP has a broad transition with a gentle slope at its northern edge and a sharper boundary with a steep slope at its eastern edge (Frost and Rost, 2014). The northern

edge of the African LLVP is steeply overturned (Ni et al., 2002). A similar feature is also observed along the northern edge of the Pacific LLVP (Li et al., 2022). Furthermore, the interactions between the slab and LLVPs may also promote aggregation or fragmentation of the compositionally distinct ultralow velocity zones (ULVZs) (Li et al., 2017), and hot upwellings due to the intense thermal instability at the edges of LLVPs, possibly resulting in hotspots and the large igneous provinces (LIPs) (Burke et al., 2008; Burke and Torsvik, 2004; Davaille et al., 2002; French and Romanowicz, 2015; Garnero and McNamara, 2008; Tan et al., 2011; Torsvik et al., 2010; Torsvik et al., 2008). Thus, deciphering the detailed seismic structures at the edge of LLVPs is crucial for understanding the composition, dynamics, and evolution in the lowermost mantle. Unlike the African LLVP, whose structures has been well constrained (Ni and Helmberger, 2003; Ni et al., 2002; Sun et al., 2007; Wang and Wen, 2007), the Pacific LLVP presents challenges in defining its detailed shape and finer scale structures, particularly at its edges (Lekic et al., 2012), due to the limited coverages of seismic ray paths.

Ray paths with events at the southern Pacific Ocean and stations in North America and Alaska allow for a great deal of investigations on seismic structures in the lowermost mantle at the northeastern and northern edge of the Pacific LLVP, respectively (Avants et al., 2006; Frost and Rost, 2014; Hutko et al., 2009; Jenkins et al., 2021; Lai et al., 2022; Lay et al., 2006; Li et al., 2022; Mori and Helmberger, 1995; Sun et al., 2019; Zhao et al., 2017). However, there have been few studies on the structures at the western edge of the Pacific LLVP (Figure S1). For example, He et al. (2006) and He and Wen (2009) detected a ULVZ (δVs = -13%, H = 30-100 km) underneath the D″ discontinuity along the edge of the Pacific LLVP. Through waveform migration, Takeuchi and Obara (2010) reported an undulated topography of the D″ discontinuity. Suzuki et al. (2020) identified some small-scale upwellings and paleoslabs using 3D waveform inversion. Despite of differences among these results, they collectively suggest that the past subduction processes have great influence on the geodynamics at the western edge of the Pacific LLVP, yielding strong thermal and chemical heterogeneities in this region. However, the 1D and 2D simulations employed in most previous studies are hard to fully capture the 3D structural variations at the western edge of the Pacific LLVP, which underscores the need of further waveform-based studies based on 3D simulations for better uncovering the interplay between the subducted materials and the Pacific LLVP.

Here, we utilize seismic data from events in the southwestern Pacific Ocean recorded by dense seismic networks along the western Pacific to study the detailed 3D structures of the western edge of the Pacific LLVP (Figure 1). With an unprecedented sampling, we first measure the differential travel times and amplitude ratios between ScS and S to locate the western boundary of the Pacific LLVP. Then, we constrain the complex seismic structures by detailed 2D and 3D waveform modeling. We observe the different structures of the Pacific LLVP in the adjacent area, which are believed to be shaped by the vigorous mantle flow associated with the actively subducted slab.

2 Data and Methods

The combination of events in the southwestern Pacific Ocean and dense stations at the China National Seismic Network (CNSN) (Data Management Center of China National Seismic Network, 2007; Zheng et al., 2009), F-net in Japan (Okada et al., 2004), and Global Seismographic Network (GSN) provides a good sampling at the western edge of the Pacific LLVP (Figure 1 and Figure S2). We select 32 events with simple source duration between 2005 and 2021 (Table 1). Raw three-component data are deconvolved with their instrument responses and bandpass filtered to 5-50 s before horizontal components rotating into radial (SV) and tangential (SH) components. Noisy seismograms are discarded by visual inspection. The tangential waveforms of events A-C are modeled in detail (Figure 1). We further stack the tangential components of events A-C in 0.5° distance bins to improve the signal-to-noise ratio (SNR) for waveform analysis. The original data of events A-C are displayed in Figures S3-S5.

Since the almost identical ray paths of S and ScS in the upper mantle (Figure S2), the ScS-S differential travel time residuals (δt_{ScS-S}) are frequently used to estimate the heterogeneities in the lowermost mantle to avoid the source location and origin time errors (He and Wen, 2012; Jenkins et al., 2021; Li et al., 2020). We first measure the δt_{ScS-S} values for tangential components with epicentral distance smaller than 85°, at which S and ScS are well separated to avoid interference between them. We also measure the ScS/S amplitude ratios ($A_{ScS/S}$) to examine the effects of different high- or low-velocity anomalies on waveform amplitudes. To eliminate the effect of radiation patterns of different events on the amplitudes of S and ScS, we calibrate $A_{ScS/S}$ as follows:

$$A_{ScS/S\ (corrected)} = \frac{A_{ScS/S\ (original)}}{A_{ScS/S\ (theoretical)}} \quad (1)$$

, where $A_{ScS/S\ (original)}$ is the measured raw amplitude ratios, $A_{ScS/S\ (theoretical)}$ is the theoretical amplitude ratios assuming source mechanism from the USGS earthquake catalogue (http://earthquake.usgs.gov), and $A_{ScS/S\ (corrected)}$ is the corrected amplitude ratios.

This amplitude correction is particularly important for data with small epicentral distance (< 80°), at which notable difference in the taking-off angles between ScS and S is present. Also, the $A_{ScS/S\ (theoretical)}$ may vary greatly among events with distinct focal mechanisms. To ensure the stable measurements of amplitudes, we retain data only with ray paths of S or ScS away from the S-wave nodal plane (Figure S6).

To better assess the effects of lateral heterogeneities on both travel time and waveforms, we perform 2D and 3D wave propagation calculations. For 2D simulations, we apply a finite-difference code, which has been widely used to generate 2D global synthetics at high frequency up to 1.0 Hz with high efficiency (Li et al., 2014). For 3D simulations, we apply the SPECFEM3ED GLOBAL package with the shortest period at ~ 4.8 s (Komatitsch et al., 2016). The event information

and focal mechanism used in the simulations are selected from the Global Centroid-Moment-Tensor (GCMT) solutions (https://www.globalcmt.org). Then, same processing procedures as for the data are applied to the synthetics.

We define misfit functions to evaluate the goodness of waveform fit between the data (D) and synthetics (S) (Li et al., 2022), to quantify how well we model the waveform. Three misfit functions including the average normalized cross-correlation coefficient (CC), L1-norm (σ_{L1}), and L2-norm (σ_{L2}) in the given time window [t_0, t_1] containing the target seismic phase are used as follows:

$$CC = \frac{1}{N}\sum_{i}^{N} CC_i(D,S) \tag{2}$$

$$\sigma_{L1} = \frac{1}{N}\sum_{i}^{N}\int_{t0}^{t1} |D_i(t) - S_i(t)|\, dt \tag{3}$$

$$\sigma_{L2} = \frac{1}{N}\sqrt{\sum_{i}^{N}\int_{t0}^{t1} (D_i(t) - S_i(t))^2\, dt} \tag{4}$$

, where N is the number of traces, D_i and S_i are aligned and normalized to S arrivals.

3 ScS-S differential travel time residuals ($\delta t_{ScS\text{-}S}$) and ScS/S amplitude ratios ($A_{ScS/S}$)

We pick S and ScS arrivals after waveforms alignment by cross-correlating for each event. In our study region, the $\delta t_{ScS\text{-}S}$'s correlate negatively with travel time residuals of S (δt_S) and positively with travel time residuals of ScS (δt_{ScS}) relative to the prediction of the 1D PREM model (Dziewonski and Anderson, 1981). The Pearson's R-values show the similar degree of correlation (Figure 2a-b), which means that $\delta t_{ScS\text{-}S}$ are controlled by both δt_{ScS} and δt_S, i.e., structures at shallower depth that sampled by S rays also contribute to $\delta t_{ScS\text{-}S}$. Thus, it is necessary to correct the travel time anomalies caused by the shallow 3D structures from tomographic models. Here, we summarize the relationships between $\delta t_{ScS\text{-}S}$ and $\delta t_{ScS}/\delta t_S$ for several tomographic models in Table 2, which suggests GyPSuM (Simmons et al., 2010) enables a better background model compared to others. We thus construct several modified GyPSuM models by substituting the Vs below a certain depth with that in the 1D PREM model. Figure S7 shows the correlations of $\delta t_S/\delta t_{ScS}$ with $\delta t_{ScS\text{-}S}$ for such modified 3D models with different depths separating the Vs in the PREM from that in the GyPSuM. When the Vs in the GyPSuM at a depth of 0-2600 km is adopted, the correlation between δt_S and δt_{ScS} with $\delta t_{ScS\text{-}S}$ becomes the weakest and strongest, respectively (Figure S7 and Figure 2c-d), suggesting that $\delta t_{ScS\text{-}S}$ anomalies are mainly from the structures in the lowermost 300 km mantle.

Figure 3a-b displays the observed δt_{ScS-S}'s projected at the ScS bouncing points at the CMB relative to PREM and GyPSuM, respectively, which exhibit complex structures at the western edge of the Pacific LLVP. Generally, the transitional boundary from positive to negative δt_{ScS-S}'s relative to GyPSuM agree with the western boundary of the Pacific LLVP mapped by He and Wen (2012) (Figure 3b). δt_{ScS-S} values are generally positive (red color in Figure 3b) in the LLVP, corresponding with the rays of ScS sampling the low-velocity LLVP. In contrast, with the rays of ScS sampling away from the LLVP, δt_{ScS-S} values become negative (blue color in Figure 3b). In the western part, around 130°E-150°E/5°S-10°N (marked by red polygon in Figure 3b), a zone with δt_{ScS-S} of ~ 1 s extends further northwest from the major LLVP anomaly, suggesting that the LLVP may extend further northwest as a limb (referred to as LLVP limb hereafter). In addition, a small-scale anomaly around 160°E/10°N with δt_{ScS-S} up to 4 s is obvious at the northwestern edge of the LLVP, which could be contributed from a localized low-velocity patch, such as ULVZ.

To intuitively show the complex structures in the lowermost 300 km above the CMB, we convert the δt_{ScS-S} values to the average δV_S and height (H) of the anomalies (Figure S8). We first smooth the measured δt_{ScS-S} values through the whole study region with a radius of caps 1°. Then, we estimate the average V_S in the lowermost 300 km above the CMB at a grid space of 0.2°×0.2° in longitude and latitude, respectively. The average H is assumed to be 300 km when we estimate the δV_S while the average δV_S is assumed to be -3% when we estimate the H. In general, the inferred δV_S ranging from -3% to 3% show a low-velocity region in the LLVP surrounded by normal- or high-velocity regions (Figure S8a). The thickness of the low-velocity layer varies from 0-300 km, with thicker layer corresponding to the lower δV_S (Figure S8b). Although no evidence for the exact δV_S and H values of anomalous structures in our study region, the general δV_S and H variations demonstrate a noticeable difference in seismic structures between inside and outside the LLVP.

Besides from δt_{ScS-S}, we further display the measured original and corrected $A_{ScS/S}$ after correction for radiation patterns, to show the relationship between the travel time anomalies and the amplitude variations in our study region (Figure 3c-d). On the whole, $A_{ScS/S}$ images before and after correction show similar patterns and correlate well with δt_{ScS-S}. Specifically, ScS rays sampling the interior of the LLVP result in elevated $A_{ScS/S}$, indicating the focusing effect of the low-velocity LLVP on the ScS wavefield.

Both δt_{ScS-S} and $A_{ScS/S}$ patterns reveal the complex structures, including low- and high-velocity patches, at the western edge of the Pacific LLVP. Besides, the distorted waveforms are also indicative of these complex structures, which are described in detail in the next section.

4 Waveform modeling

4.1 Anomalous ScS and Scd waveforms

Events A and B, located along the similar great circle path from Tonga-Fiji to China, provide an opportunity to better constrain the detailed structure at the western edge of the Pacific LLVP (Figure 1 and Figure 4). According to the features of waveforms, we subdivide the data of events A and B into two adjacent azimuths: profile I, in the azimuth range of 300°-305°; profile II, in the azimuth range of 305°-310°. The azimuth is taken from event A (Figure 4c).

On profile I, the rays sample along the LLVP limb (Figure 4). Compared to those on profile II, ScS arrivals of event A at the distance ranging from 85° to 93° on profile I exhibits significant delays and with large amplitudes (Figure 5a, c). Because the ray paths of S and ScS are almost identical except for the lowermost mantle at the distance of ~ 90° (Figure 4a), the strongly delayed ScS supports the existence of the low-velocity LLVP limb. On profile II, extra arrivals are visible between S and ScS at the distance of 80°-85° (Figure 5c), which are commonly explained as the Scd phase generated by a D″ discontinuity (He and Wen, 2012; He et al., 2006; Ko et al., 2017; Li et al., 2021; Sun et al., 2016; Thomas et al., 2004). Additionally, at the distance of 88°-95°, S waveforms of event B show two arrivals on profile II (Figure 5d and Figure 6). Due to the proximity of the sampling area for events A and B (Figure 4b), we regard the anomalous S waveforms of event B as the interference of Scd with direct S arrival at large distance.

The notable difference in SH waveforms between the adjacent azimuths described above suggests that the velocity structures are characterized by rapid changes at the western edge of the Pacific LLVP. In the following sections, we attempt to construct a 3D model to fit the observed anomalous waveforms and discuss the interactions among the complex structures.

4.2 Complex structures at the western edge of the Pacific LLVP

To fit the observed anomalous waveforms, we embed additional structures in the lowermost mantle outlined by the anomalous δt_{ScS-S} values into the GyPSuM. For simplicity, we start with modeling waveforms of events A and B along profiles I and II separately with 2D simulations. Then, we perform 3D simulations for events A, B and C to further demonstrate the complex structures in our study region.

4.2.1 LLVP limb

In 2D simulations, GyPSuM model has difficulty to predict the delayed ScS across the whole distance range, particularly for the ScS waveforms with large amplitudes at the distance of 85°-93° and the broadening S waveforms at the distance of ~ 95° of event A on profile I (Figure 5a). At the distance smaller than 80°, the ScS bouncing points fall into the proximity of region with negative δV_S in the GyPSuM on

profile I (Figure 4a), we thus establish a model that enhances the negative δV_S by 1.5 times at 700 km above the CMB in the GyPSuM (referred to as the enhanced GyPSuM hereafter). The 700 km above the CMB selected here is accordance with the height of the Pacific LLVP in the GyPSuM. The enhanced GyPSuM provides a good fit to the delayed ScS at the distance smaller than 85° (Figure S9a), but not at larger distance because the δV_S where the ScS bouncing points fall into are too weak to reproduce the delayed ScS with large amplitudes (Figure 4a). By incorporating the LLVP limb in Figure 3b into the enhanced GyPSuM on profile I, the anomalous ScS of event A in both travel time and amplitude can be predicted well (Figure 5a). Here, the anomalous δt_{ScS-S} shown in Figure 3b outlines the extent of the LLVP limb being at the distance of 40°-55° with respect to event A. For event B, the rays of ScS sample the LLVP limb at the distance smaller than 80° with more vertical incidence (Figure 4a), and the synthetics for the hybrid model only display slightly delayed ScS with no obvious waveform distortion due to the relatively weak δV_S in the LLVP limb, which agree with the data (Figure 5b).

Given that the lateral extent of the LLVP limb has been confined, we further attempt to constrain the δV_S and H of the LLVP limb. The ScS waveforms of event A are more sensitive to the velocity perturbations in the LLVP limb, compared to those of event B. Thus, to examine the robustness of the parameters of the LLVP limb, we only use event A to quantify how different values of the δV_S and H of the LLVP limb can affect the goodness of fit of ScS waveforms on profile I. We grid search the optimal values for δV_S, ranging from -30% to 0 with 1% interval relative to the PREM, and for H, varying from 0-300 km with 10 km interval. Figure 7 shows that different misfit functions, i.e. CC, σ_{L1}, and σ_{L2}, between the data and synthetics give similar patterns, in which strong trade-off between δV_S and H exists. The CC values are high (σ_{L1} or σ_{L2} values are low) when the product of δV_S and H is close to -1.2 km. Figure S10 displays synthetics for several LLVP limb models with a product of δV_S and H being -1.2 km. If the δV_S is stronger than -6%, strong arrivals resulting from multiple reflections in the LLVP limb layer following ScS are developed, and the S waveforms at large distance get broader. On the other hand, when the δV_S is weak and H is large (i.e. δV_S = -2%, H = 60 km), the amplitude of the ScS is rather small, compared to the data, at the distance of 90°-93°. In summary, despite the large uncertainties, a LLVP limb model with δV_S = -4%, H = 30 km can provide a reasonable fit for both the travel time and large amplitudes of ScS at the distance of 90°-93°. Besides from the δV_S and H, synthetics also show negligible waveform difference for a box- and triangle-shaped model, implying another trade-off between the shapes of the LLVP limb (Figure S11).

4.2.2 D″ layer

Similar to that on profile I, we also enhance the negative δV_S in the LLVP region on profile II (Figure 4b), which fits the delayed ScS of event A well (Figure S9b). However, it cannot generate the double arrivals, comprising Scd and S waveforms, observed at the distance of 88°-95° of event B (Figure 6). Thus, we test models by

introducing a high-velocity D″ layer into the enhanced GyPSuM on profile II (Figure 4b). Here, we fix the lateral size of the D″ layer based on δt_{ScS-S} in Figure 3b and grid search the δV_S across the D″ discontinuity and height of the D″ layer (Figure 8), which vary from 0 to +6% and 0-500 km, respectively. For simplification, we only consider the D″ layer structure with a D″ discontinuity in which the δV_S gradually varied with depth (Figure 8). The *CC*, σ_{L1}, or σ_{L2} values all suggest that a model with δV_S varying gradually from +2.2% at the D″ discontinuity, 320 km above the CMB, to 0 at the CMB is optimal to replicate the anomalous Scd+S waveforms of event B on profile II, even for the depth phase sS (Figure 6 and Figure 8).

On profile II, the D″ layer also produces Scd arrivals between S and ScS at the distance of 80°-85° of event A (Figure 5c) and 75°-80° of event B (Figure 5d) in synthetics. Due to the interference of SKS arrivals caused by the anisotropic effect and possible S reverberations within the crust, it is difficult to directly identify the Scd at the distance smaller than 85° in the waveform data. Nevertheless, the Scd arrivals at these distance ranges are distinctly observable in the vespagrams (Figure S12).

4.2.3 hybrid 3D structure

Based on the developed 2D structures above, we construct a hybrid 3D model by incorporating the LLVP limb and additional D″ regions, D″-1 and D″-2 as shown in Figure 3b, into the enhanced GyPSuM. The southwestern boundary of the D″-1 structure is aligned with the azimuth of 305° relative to event A (Figure 3b). However, its northeastern boundary cannot be well resolved due to the limited data coverage. We approximate its northeastern boundary as the transitional boundary of the δt_{ScS-S} values changing from negative (blue color) to zero (green color) in Figure 3b, roughly following the azimuth of 315° of event A. The southwestern boundary of the D″-1 structure can also be well constrained by the rapid variation in S waveforms with the azimuth of event B (Figure S13). The D″-2 structure largely coincides with the D″ model sampled in He et al. (2006) (Figure S14). Thus, we simply adopt their D″ model, in which the δV_S across the D″ discontinuity is +2% and the *H* is 100-145 km. The boundaries of the D″-2 structure are also approximately delineated based on the measurement of the δt_{ScS-S} (Figure 3b).

For event A, the synthetics generated by the 3D hybrid model generally agree with the data across all azimuth ranges (Figure 9). Moreover, the 3D hybrid model with sharp boundaries among the LLVP limb, the D″ region, and the ambient mantle successfully reproduce the drastic variations in ScS waveforms with changing azimuths (Figure 10). In contrast, a LLVP limb model with smooth boundary cannot capture such strong waveform variations (Figure 10 and Figure S15). For event B, the Scd+S waveforms are fitted well by introducing the D″ structure in 3D hybrid model, as well as for the depth phase sS followed by S (Figure 11 and Figure S16). For event C, the rays sample the D″-1 structure within the azimuth range of 300°-310° and the D″-2 structure at the azimuth larger than 310° (Figure S14). The synthetics generated by the 3D hybrid model exhibit distinct Scd arrivals at the distance of ~ 80°, in

contrast to those produced from the GyPSuM (Figures S17-S18). In the azimuth range of 290°-300°, the Scd is not present due to the related ray paths missing the D″ structures, but the ScS arrivals are delayed, which can be accounted for rays sampling the low-velocity LLVP limb. Similar to event A, our 3D hybrid model also fit the ScS well for the trend of abruptly changing from normal to delayed waveforms at the azimuth of ~ 300° for event C (Figure S19). Well matched ScS and Scd waveforms on azimuth profiles of events A, B, and C suggest a sharp transitional boundary among the LLVP limb, the D″-1 region and the ambient mantle, as well as the robustness of our proposed 3D hybrid model despite the possible existence of small-scale heterogeneities.

5 Discussion

5.1 Evaluation of the hybrid model

Our hybrid model not only enhances the negative δV_S in the LLVP region, but includes the LLVP limb and the high-velocity D″ layer at the base of the mantle based on the GyPSuM (see section 4.2). Besides from the differential travel times between ScS and S, the complex structural variations in our hybrid model may have effect on S travel time. Seismograms of event A and event B on profile I and profile II aligned on S predicted by PREM show that our proposed hybrid model is more capable of reproducing the S arrivals changing with distance, compared to GyPSuM (Figures S20-S21). In particular, the low-velocity LLVP limb contributes to the significant delays of Sdiff of event A at larger distance. Moreover, to show the effect of structures in the shallow mantle on S arrival times, we test another model that only includes heterogeneities at 700 km above the CMB and replaces V_S values with those in the PREM at 0-2200 km. Synthetics for this modified model suggest that S arrival times have the parallel trend as those predicted by our hybrid model on distance profiles despite of some difference in magnitude (Figure S22), implying that the S arrival time variations in the data mostly originate from the heterogeneities in the lowermost mantle. The complex structures we detected in the lowermost mantle are also independent with the tomographic model. Generally, our hybrid 2D and 3D models are able to generate the anomalous waveforms as the data for selected events that sample the different structures, suggesting the complex structures with sharp boundaries at the western edge of the Pacific LLVP. However, there are some deficiencies for our hybrid model in waveform modeling.

Neither our hybrid 2D nor 3D model can reproduce the ScS with exceptionally large amplitude at the distance of 90°-93° of event A on profile I (Figure 5a and Figure 9a). There are several possible causes that may account for the large amplitude of ScS. The source may come from the weaker amplitudes of S waveforms when S rays sampling the particular structure, resulting in the stronger ScS when waveforms are normalized. Alternatively, our LLVP limb model with a homogeneous δV_S and a

box-like shape may oversimplify the existence of small-scale heterogeneities and more complicated shape. Besides, our hybrid model also has difficulty to model the extremely weak ScS amplitudes at the distance of 75°-80° of event B on profile II (Figure 5d and Figure S16). Such weak ScS amplitudes may be indicative of more complicated internal structures in the D″-1 layer which may have high attenuation for the ScS energy. We also test models with different localized small-scale types of the CMB topography to show the effects on ScS arrival times and amplitudes (Figure S23). It suggests that the concave downward shape and the convex upward shape may play a limited role in increasing and decreasing the ScS amplitudes, respectively. Nevertheless, given the depth scale of the CMB topography is only several kilometers (Earle and Shearer, 1997; Sze and van der Hilst, 2003), it is unlikely to be the main source of the observed anomalous ScS arrival times and extreme ScS amplitudes. To better resolve these finer-scale structures, it is crucial to include more seismic data that samples the LLVP limb with ray paths parallel to the LLVP boundary. However, at current stage, additional constraints on the LLVP limb cannot be provided.

The synthetic Scd arrivals for 3D hybrid model in the azimuth range of 310°-330° of event C are generated due to the rays sampling the D″-2 structure (Figures S14, S18). However, the Scd arrivals are visible only in the azimuth range of 315°-320° and 325°-330° in the vespagrams (Figure S24), which may suggest that the D″-2 region is composed of several disconnected D″ structures. The amplitudes of Scd in the azimuth range of 315°-320° are also much larger than those in the azimuth range of 325°-330° in the data (Figure S18), further indicating a more complicated D″-2 structure.

In summary, although our hybrid model has limitations in modeling the waveform data in finer detail, it efficiently captures the first-order features of the complex structures with sharp transitional boundaries at the western edge of the Pacific LLVP.

5.2 Existence of ULVZ at the western edge of the Pacific LLVP?

ULVZs have been routinely found at the northern, northeastern, and eastern edges of the Pacific LLVP (Avants et al., 2006; Jenkins et al., 2021; Lai et al., 2022; Li et al., 2022; Luo et al., 2001; Ma et al., 2019; Mori and Helmberger, 1995; Revenaugh and Meyer, 1997; Sun et al., 2019; Zhao et al., 2017). At the western edge, He et al. (2006) and He and Wen (2009) report the presence of a ULVZ beneath the D″ layer by modeling the SuS arrival, which is generated from the reflection atop the ULVZ and has the opposite polarity to ScS. In this study, the rays of event C within the azimuth range of 310°-320° sample the same region as in He et al. (2006) (Figure S14). However, no coherent SuS arrival can be identified in our data (Figures S17-S18). One possibility for this discrepancy is that our analysis primarily relies on relatively long period data (> 5 s), thereby not detecting the ULVZ here. In essence, it is plausible that a thin ULVZ exists but below the detection threshold of our data. In addition, Thorne et al. (2021) image some possible large-scale ULVZs with high probability by

anomalous SPdKS waveforms. These ULVZs are uncertain because their locations have ambiguity between source side and receiver side where Pd segment diffracts along the CMB. If these ULVZs exist, they are exactly located inside the Pacific LLVP (Figure S1). However, our data cannot validate these ULVZs due to the limited ray path coverage. We acknowledge that some localized small-scale ULVZs are possibly present in our study region revealed by the large δt_{ScS-S}, and waveform analysis for recordings at a small-aperture array is necessary to identify them.

5.3 Interactions among the complex structures at the western edge of the Pacific LLVP

In our model, the low-velocity LLVP limb situated at the western edge of the Pacific LLVP has a lateral size of ~ 900×600 km and a height of 30 km. Synthetics suggest that the delayed ScS waveforms at the distance of ~ 90° cannot be modeled by the isolated LLVP limb model (i.e., the LLVP limb is away from the Pacific LLVP) (Figure S25). Moreover, the δV_S of the LLVP limb is also comparable to that of the enhanced GyPSuM, implying a possible scenario where this limb structure extends from the main Pacific LLVP. To the north of the LLVP limb, the presence of two D″ regions (Figure 3b) may suggest the existence of a subducted slab near the western edge of the Pacific LLVP, as the formation of the observed D″ discontinuity could be closely linked to the phase transition from bridgmanite to post-bridgmanite in a cold subduction environment (Murakami et al., 2004; Murakami et al., 2005; Oganov and Ono, 2004; Sun et al., 2018). Moreover, the difference in structures between D″-1 and D″-2 layers, such as height and the magnitude of δV_S, may suggest significant complexity in temperature or/and composition between them when slab entering into the lowermost mantle.

Knowledge of the structures of the edge of LLVPs will be conductive to evaluate the dynamic process in the lowermost mantle. For the Pacific LLVP, S-wave studies show that the Pacific LLVP has both steep and gentle sides at the western and northern edge (He and Wen, 2009, 2012), and P-wave study suggests a steep and sharp eastern edge, and a shallow and more diffuse northern edge of the Pacific LLVP (Frost and Rost, 2014). The dynamic models imply that the mantle flow associated with the subducted slab in the lower mantle plays a critical role in shaping the LLVP (McNamara and Zhong, 2005). Based on our observations of various structures along the different profiles here (Figure 4a-b), we hypothesize that the structures of the western edge of the Pacific LLVP are largely affected by the mantle flow associated with the subducted slab in the lowermost mantle. In the southern part of our study region, along profile I, although tomographic model shows high-velocity patch near the LLVP limb (Figure 4a), the undetected D″ layer based on the observations may suggest the slab on this profile is absent, which allows the LLVP to extend further outward as a LLVP limb with a low height (Figure 12a). In contrast, in the northern part (profile II), the LLVP experiences significant pushing by the subducted slab, which shapes the LLVP into a dome-like structure without a LLVP limb structure (Figure 12b). The

sharp boundary among the LLVP limb, the D″ layer and the ambient mantle may suggest that it is plausibly a region with high thermal gradients, which is likely indicative of an active subduction where crust and lithosphere has recently been subducted. In addition, the presence of the slab may introduce more complicated 3D mantle flow, exerting further influence on the 3D structure of the Pacific LLVP. This hypothesis is expected to be verified in the future geodynamic simulations.

6 Conclusion

In this study, we provide a detailed image at the western edge of the Pacific LLVP by dense seismic recordings. We outline the S-wave western boundary of the Pacific LLVP by the measured travel time and amplitude anomalies between ScS and S. The western boundary of the Pacific LLVP is similar to that in a previous study, except for a northwestward extended LLVP region. Besides, the high-velocity D″ layer structures which are associated with the subducted slab are widely distributed outside the Pacific LLVP. Drastically varied waveforms on azimuth profiles from different events all suggest a sharp transitional boundary among the complex structures. Furthermore, we determine the complex S-wave velocity structures by detailed 2D and 3D waveform modeling. After comparing the different velocity structures within the adjacent region, we propose that the 3D structures of the western edge of the Pacific LLVP are strongly influenced by the vigorous mantle flow associated with the actively subducted slab.

Acknowledgements

We are grateful to the Editor Michael Bostock for the editorial handling and to the Associate Editor and two anonymous reviewers for their constructive suggestions. The authors would like to thank the Data Management Centre of China National Seismic Network at Institute of Geophysics, China Earthquake Administration, the NIED F-net Broadband Seismograph Network in Japan, and Global Seismographic Network in IRIS Data Center for providing the high-quality seismic data. J.L. was supported by the National Natural Science Foundation of China under grant NSFC42304102, the “CUG Scholar” Scientific Research Funds at China University of Geoscience (Wuhan) (No. 2022150), the Postdoctoral Fellowship Program of CPSF (No. 2023M733293), and the State Key Laboratory of Geodesy and Earth’s Dynamics open fund under grant SKLGED2023-4-4. The authors appreciate the Supercomputing Center of USTC for high-performance computing services.

Open Research

Waveform data used in this study are obtained from the China National Seismic Network (CNSN) (Data Management Center of China National Seismic Network,

2007; Zheng et al., 2009), the NIED F-net Broadband Seismograph Network (Okada et al., 2004), and the Global Seismographic Network (GSN) (Albuquerque Seismological Laboratory/USGS, 2014). All waveform data used for travel time residuals and amplitude ratios measurement and for waveform modeling in this study are available at Zenodo (Li et al., 2024). All maps in this paper were produced using GMT developed by Paul Wessel and Walter H.F. Smith.

References

Albuquerque Seismological Laboratory/USGS. (2014). Global Seismograph Network (GSN – IRIS/USGS). International Federation of Digital Seismograph Networks [Dataset]. https://doi.org/10.7914/SN/IU

Avants, M., Lay, T., Garnero, E.J., 2006. A new probe of ULVZ S-wave velocity structure: Array stacking of ScS waveforms. *Geophysical Research Letters*, 33. https://doi.org/10.1029/2005gl024989

Boyet, M., Carlson, R.W., 2005. Nd-142 evidence for early (> 4.53 Ga) global differentiation of the silicate Earth. *Science*, 309, 576-581. https://doi.org/10.1126/science.1113634

Burke, K., Steinberger, B., Torsvik, T.H., Smethurst, M.A., 2008. Plume generation zones at the margins of large low shear velocity provinces on the core-mantle boundary. *Earth and Planetary Science Letters*, 265, 49-60. https://doi.org/10.1016/j.epsl.2007.09.042

Burke, K., Torsvik, T.H., 2004. Derivation of Large Igneous Provinces of the past 200 million years from long-term heterogeneities in the deep mantle. *Earth and Planetary Science Letters*, 227, 531-538. https://doi.org/10.1016/j.epsl.2004.09.015

Carlson, R.W., Boyet, M., 2006. Long-term consequences of early earth differentiation. *Geochimica et Cosmochimica Acta Supplement*, 70, A84-A84. https://doi.org/10.1016/j.gca.2006.06.080

Data Management Center of China National Seismic Network. (2007). Waveform data of China National Seismic Network [Dataset]. *Institute of Geophysics, China Earthquake Administration.* http://esdc.ac.cn/

Davaille, A., Girard, F., Le Bars, M., 2002. How to anchor hotspots in a convecting mantle? *Earth and Planetary Science Letters*, 203, 621-634. https://doi.org/10.1016/S0012-821x(02)00897-X

Davies, D.R., Goes, S., Davies, J.H., Schuberth, B.S.A., Bunge, H.P., Ritsema, J., 2012. Reconciling dynamic and seismic models of Earth's lower mantle: The dominant role of thermal heterogeneity. *Earth and Planetary Science Letters*, 353, 253-269. https://doi.org/10.1016/j.epsl.2012.08.016

Dziewonski, A.M., Anderson, D.L., 1981. Preliminary Reference Earth Model. *Physics of the Earth and Planetary Interiors*, 25, 297-356. https://doi.org/10.1016/0031-9201(81)90046-7

Earle, P.S., Shearer, P.M., 1997. Observations of PKKP precursors used to estimate small-scale topography on the core-mantle boundary. *Science*, 277, 667-670. https://doi.org/10.1126/science.277.5326.667

French, S.W., Romanowicz, B., 2015. Broad plumes rooted at the base of the Earth's mantle beneath major hotspots. *Nature*, 525, 95-99. https://doi.org/10.1038/nature14876

565 Frost, D.A., Rost, S., 2014. The P-wave boundary of the Large-Low Shear Velocity
566 Province beneath the Pacific. *Earth and Planetary Science Letters*, 403, 380-392.
567 https://doi.org/10.1016/j.epsl.2014.06.046
568 Garnero, E.J., Helmberger, D.V., 1995. A Very Slow Basal Layer Underlying
569 Large-Scale Low-Velocity Anomalies in the Lower Mantle beneath the Pacific -
570 Evidence from Core Phases. *Physics of the Earth and Planetary Interiors*, 91,
571 161-176. https://doi.org/10.1016/0031-9201(95)03039-Y
572 Garnero, E.J., McNamara, A.K., 2008. Structure and dynamics of Earth's lower mantle.
573 *Science*, 320, 626-628. https://doi.org/10.1126/science.1148028
574 Grand, S.P., 2002. Mantle shear-wave tomography and the fate of subducted slabs.
575 *Philosophical Transactions of the Royal Society of London. Series A:*
576 *Mathematical, Physical and Engineering Sciences*, 360, 2475-2491.
577 https://doi.org/10.1098/rsta.2002.1077
578 He, Y.M., Wen, L.X., 2009. Structural features and shear-velocity structure of the
579 "Pacific Anomaly". *Journal of Geophysical Research-Solid Earth*, 114.
580 https://doi.org/10.1029/2008jb005814
581 He, Y.M., Wen, L.X., 2012. Geographic boundary of the "Pacific Anomaly" and its
582 geometry and transitional structure in the north. *Journal of Geophysical*
583 *Research-Solid Earth*, 117. https://doi.org/10.1029/2012jb009436
584 He, Y.M., Wen, L.X., Zheng, T.Y., 2006. Geographic boundary and shear wave
585 velocity structure of the "Pacific anomaly" near the core-mantle boundary beneath
586 western Pacific. *Earth and Planetary Science Letters*, 244, 302-314.
587 https://doi.org/10.1016/j.epsl.2006.02.007
588 Houser, C., Masters, G., Shearer, P., Laske, G., 2008. Shear and compressional velocity
589 models of the mantle from cluster analysis of long-period waveforms.
590 *Geophysical Journal International*, 174, 195-212.
591 https://doi.org/10.1111/j.1365-246X.2008.03763.x
592 Hutko, A.R., Lay, T., Revenaugh, J., 2009. Localized double-array stacking analysis of
593 PcP: D" and ULVZ structure beneath the Cocos plate, Mexico, central Pacific, and
594 north Pacific. *Physics of the Earth and Planetary Interiors*, 173, 60-74.
595 https://doi.org/10.1016/j.pepi.2008.11.003
596 Ishii, M., Tromp, J., 1999. Normal-mode and free-air gravity constraints on lateral
597 variations in velocity and density of Earth's mantle. *Science*, 285, 1231-1236.
598 https://doi.org/10.1126/science.285.5431.1231
599 Ishii, M., Tromp, J., 2001. Even-degree lateral variations in the Earth's mantle
600 constrained by free oscillations and the free-air gravity anomaly. *Geophysical*
601 *Journal International*, 145, 77-96.
602 https://doi.org/10.1046/j.1365-246x.2001.00385.x
603 Ishii, M., Tromp, J., 2004. Constraining large-scale mantle heterogeneity using mantle
604 and inner-core sensitive normal modes. *Physics of the Earth and Planetary*
605 *Interiors*, 146, 113-124. https://doi.org/10.1016/j.pepi.2003.06.012

606 Jenkins, J., Mousavi, S., Li, Z., Cottaar, S., 2021. A high-resolution map of Hawaiian
607 ULVZ morphology from ScS phases. *Earth and Planetary Science Letters*, 563.
608 https://doi.org/10.1016/j.epsl.2021.116885
609 Ko, J.Y.-T., Hung, S.-H., Kuo, B.-Y., Zhao, L.J.E., Letters, P.S., 2017. Seismic
610 evidence for the depression of the D″ discontinuity beneath the Caribbean:
611 Implication for slab heating from the Earth's core. *Earth and Planetary Science*
612 *Letters*, 467, 128-137. https://doi.org/10.1016/j.epsl.2017.03.032
613 Koelemeijer, P., Deuss, A., Ritsema, J., 2017. Density structure of Earth's lowermost
614 mantle from Stoneley mode splitting observations. *Nature Communications*, 8.
615 https://doi.org/10.1038/ncomms15241
616 Koelemeijer, P., Ritsema, J., Deuss, A., van Heijst, H.J., 2016. SP12RTS: a degree-12
617 model of shear- and compressional-wave velocity for Earth's mantle. *Geophysical*
618 *Journal International*, 204, 1024-1039. https://doi.org/10.1093/gji/ggv481
619 Komatitsch, D., Xie, Z.N., Bozdag, E., de Andrade, E.S., Peter, D., Liu, Q.Y., Tromp,
620 J., 2016. Anelastic sensitivity kernels with parsimonious storage for adjoint
621 tomography and full waveform inversion. *Geophysical Journal International*,
622 206, 1467-1478. https://doi.org/10.1093/gji/ggw224
623 Lai, V.H., Helmberger, D., Dobrosavljevic, V., Wu, W., Sun, D., Jackson, J.M., Gurnis,
624 M., 2022. Strong ULVZ and Slab Interaction at the Northeastern Edge of the
625 Pacific LLSVP Favors Plume Generation. *Geochemistry, Geophysics,*
626 *Geosystems*, 23. https://doi.org/10.1029/2021GC010020
627 Lau, H.C.P., Mitrovica, J.X., Davis, J.L., Tromp, J., Yang, H.Y., Al-Attar, D., 2017.
628 Tidal tomography constrains Earth's deep-mantle buoyancy. *Nature*, 551,
629 321-326. https://doi.org/10.1038/nature24452
630 Lay, T., Hernlund, J., Garnero, E.J., Thorne, M.S., 2006. A post-perovskite lens and D"
631 heat flux beneath the central Pacific. *Science*, 314, 1272-1276.
632 https://doi.org/10.1126/science.1133280
633 Lei, W.J., Ruan, Y.Y., Bozdag, E., Peter, D., Lefebvre, M., Komatitsch, D., Tromp, J.,
634 Hill, J., Podhorszki, N., Pugmire, D., 2020. Global adjoint tomography—model
635 GLAD-M25. *Geophysical Journal International*, 223, 1-21.
636 https://doi.org/10.1093/gji/ggaa253
637 Lekic, V., Cottaar, S., Dziewonski, A., Romanowicz, B., 2012. Cluster analysis of
638 global lower mantle tomography: A new class of structure and implications for
639 chemical heterogeneity. *Earth and Planetary Science Letters*, 357, 68-77.
640 https://doi.org/10.1016/j.epsl.2012.09.014
641 Li, D.Z., Helmberger, D., Clayton, R.W., Sun, D.Y., 2014. Global synthetic
642 seismograms using a 2-D finite-difference method. *Geophysical Journal*
643 *International*, 197, 1166-1183. https://doi.org/10.1093/gji/ggu050
644 Li, G.H., Bai, L., Ritsema, J., 2020. Lateral Variations of Shear-Wave Velocity in the
645 D" Layer Beneath the Indian-Eurasian Plate Collision Zone. *Geophysical*
646 *Research Letters*, 47. https://doi.org/10.1029/2019GL086856

Li, J.W., Zhang, B.L., Sun, D.Y., Tian, D.D., Yao, J.Y., 2024. Detailed 3D structures of the western edge of the Pacific Large Low Velocity Province [Dataset]. Zenodo. https://zenodo.org/records/10521032

Li, J.W., Sun, D.Y., Bower, D.J., 2022. Slab control on the mega-sized North Pacific ultra-low velocity zone. *Nature Communications*, 13. https://doi.org/10.1038/s41467-022-28708-8

Li, M.M., McNamara, A.K., Garnero, E.J., Yu, S.L., 2017. Compositionally-distinct ultra-low velocity zones on Earth's core-mantle boundary. *Nature Communications*, 8. https://doi.org/10.1038/s41467-017-00219-x

Li, Y.W., Miller, M.S., Tkalcic, H., Sambridge, M., 2021. Small-scale heterogeneity in the lowermost mantle beneath Alaska and northern Pacific revealed from shear-wave triplications. *Earth and Planetary Science Letters*, 559. https://doi.org/10.1016/j.epsl.2021.116768

Lu, C., Grand, S.P., Lai, H.Y., Garnero, E.J., 2019. TX2019slab: A New P and S Tomography Model Incorporating Subducting Slabs. *Journal of Geophysical Research-Solid Earth*, 124, 11549-11567. https://doi.org/10.1029/2019jb017448

Luo, S.N., Ni, S.D., Helmberger, D.V., 2001. Evidence for a sharp lateral variation of velocity at the core-mantle boundary from multipathed PKPab. *Earth and Planetary Science Letters*, 189, 155-164. https://doi.org/10.1016/S0012-821x(01)00364-8

Ma, X.L., Sun, X.L., Thomas, C., 2019. Localized ultra-low velocity zones at the eastern boundary of Pacific LLSVP. *Earth and Planetary Science Letters*, 507, 40-49. https://doi.org/10.1016/j.epsl.2018.11.037

McNamara, A.K., Zhong, S.J., 2005. Thermochemical structures beneath Africa and the Pacific Ocean. *Nature*, 437, 1136-1139. https://doi.org/10.1038/nature04066

Megnin, C., Romanowicz, B., 2000. The three-dimensional shear velocity structure of the mantle from the inversion of body, surface and higher-mode waveforms. *Geophysical Journal International*, 143, 709-728. https://doi.org/10.1046/j.1365-246X.2000.00298.x

Mori, J., Helmberger, D.V., 1995. Localized Boundary-Layer Below the Mid-Pacific Velocity Anomaly Identified from a PcP Precursor. *Journal of Geophysical Research-Solid Earth*, 100, 20359-20365. https://doi.org/10.1029/95jb02243

Murakami, M., Hirose, K., Kawamura, K., Sata, N., Ohishi, Y., 2004. Post-perovskite phase transition in $MgSiO_3$. *Science*, 304, 855-858. https://doi.org/10.1126/science.1095932

Murakami, M., Hirose, K., Sata, N., Ohishi, Y., 2005. Post-perovskite phase transition and mineral chemistry in the pyrolitic lowermost mantle. *Geophysical Research Letters*, 32. https://doi.org/10.1029/2004gl021956

Ni, S.D., Helmberger, D.V., 2003. Seismological constraints on the South African superplume; could be the oldest distinct structure on Earth. *Earth and Planetary Science Letters*, 206, 119-131. https://doi.org/10.1016/S0012-821x(02)01072-5

688 Ni, S.D., Helmberger, D.V., Tromp, J., 2005. Three-dimensional structure of the
689 African superplume from waveform modelling. *Geophysical Journal*
690 *International*, 161, 283-294. https://doi.org/10.1111/j.1365-246X.2005.02508.x
691 Ni, S.D., Tan, E., Gurnis, M., Helmberger, D., 2002. Sharp sides to the African
692 superplume. *Science*, 296, 1850-1852. https://doi.org/10.1126/science.1070698
693 Oganov, A.R., Ono, S., 2004. Theoretical and experimental evidence for a
694 post-perovskite phase of MgSiO3 in Earth's D" layer. *Nature*, 430, 445-448.
695 https://doi.org/10.1038/nature02701
696 Okada, Y., Kasahara, K., Hori, S., Obara, K., Sekiguchi, S., Fujiwara, H., Yamamoto,
697 A., 2004. Recent progress of seismic observation networks in Japan - Hi-net,
698 F-net, K-NET and KiK-net [Dataset]. *Earth Planets Space*, 56, Xv-Xxviii.
699 https://doi.org/10.1186/Bf03353076
700 Revenaugh, J., Meyer, R., 1997. Seismic evidence of partial melt within a possibly
701 ubiquitous low-velocity layer at the base of the mantle. *Science*, 277, 670-673.
702 https://doi.org/10.1126/science.277.5326.670
703 Richards, M.A., Engebretson, D.C., 1992. Large-Scale Mantle Convection and the
704 History of Subduction. *Nature*, 355, 437-440. https://doi.org/10.1038/355437a0
705 Ritsema, J., Deuss, A., van Heijst, H.J., Woodhouse, J.H., 2011. S40RTS: a degree-40
706 shear-velocity model for the mantle from new Rayleigh wave dispersion,
707 teleseismic traveltime and normal-mode splitting function measurements.
708 *Geophysical Journal International*, 184, 1223-1236.
709 https://doi.org/10.1111/j.1365-246X.2010.04884.x
710 Romanowicz, B., 2001. Can we resolve 3D density heterogeneity in the lower mantle?
711 *Geophysical Research Letters*, 28, 1107-1110.
712 https://doi.org/10.1029/2000gl012278
713 Schuberth, B.S.A., Bunge, H.P., Ritsema, J., 2009. Tomographic filtering of
714 high-resolution mantle circulation models: Can seismic heterogeneity be
715 explained by temperature alone? *Geochemistry, Geophysics, Geosystems*, 10.
716 https://doi.org/10.1029/2009gc002401
717 Simmons, N.A., Forte, A.M., Boschi, L., Grand, S.P., 2010. GyPSuM: A joint
718 tomographic model of mantle density and seismic wave speeds. *Journal of*
719 *Geophysical Research-Solid Earth*, 115. https://doi.org/10.1029/2010jb007631
720 Simmons, N.A., Myers, S.C., Johannesson, G., Matzel, E., 2012. LLNL-G3Dv3:
721 Global P wave tomography model for improved regional and teleseismic travel
722 time prediction. *Journal of Geophysical Research-Solid Earth*, 117.
723 https://doi.org/10.1029/2012jb009525
724 Sun, D., Helmberger, D., Lai, V.H., Gurnis, M., Jackson, J.M., Yang, H.Y., 2019. Slab
725 Control on the Northeastern Edge of the Mid-Pacific LLSVP Near Hawaii.
726 *Geophysical Research Letters*, 46, 3142-3152.
727 https://doi.org/10.1029/2018gl081130
728 Sun, D., Tan, E., Helmberger, D., Gurnis, M., 2007. Seismological support for the
729 metastable superplume model, sharp features, and phase changes within the lower

mantle. *Proceedings of the National Academy of Sciences*, 104, 9151-9155. https://doi.org/10.1073/pnas.0608160104

Sun, D.Y., Helmberger, D., Miller, M.S., Jackson, J.M., 2016. Major disruption of D" beneath Alaska. *Journal of Geophysical Research-Solid Earth*, 121, 3534-3556. https://doi.org/10.1002/2015jb012534

Sun, N.Y., Wei, W., Han, S.J., Song, J.H., Li, X.Y., Duan, Y.F., Prakapenka, V.B., Mao, Z., 2018. Phase transition and thermal equations of state of (Fe, Al)-bridgmanite and post-perovskite: Implication for the chemical heterogeneity at the lowermost mantle. *Earth and Planetary Science Letters*, 490, 161-169. https://doi.org/10.1016/j.epsl.2018.03.004

Suzuki, Y., Kawai, K., Geller, R.J., Tanaka, S., Siripunvaraporn, W., Boonchaisuk, S., Noisagool, S., Ishihara, Y., Kim, T., 2020. High-resolution 3-D S-velocity structure in the D" region at the western margin of the Pacific LLSVP: Evidence for small-scale plumes and paleoslabs. *Physics of the Earth and Planetary Interiors*, 307. https://doi.org/10.1016/j.pepi.2010.06.002

Sze, E.K.M., van der Hilst, R.D., 2003. Core mantle boundary topography from short period PcP, PKP, and PKKP data. *Physics of the Earth and Planetary Interiors*, 135, 27-46. https://doi.org/10.1016/S0031-9201(02)00204-2

Takeuchi, N., Obara, K., 2010. Fine-scale topography of the D" discontinuity and its correlation to volumetric velocity fluctuations. *Physics of the Earth and Planetary Interiors*, 183, 126-135. https://doi.org/10.1016/j.pepi.2010.06.002

Tan, E., Leng, W., Zhong, S.J., Gurnis, M., 2011. On the location of plumes and lateral movement of thermochemical structures with high bulk modulus in the 3-D compressible mantle. *Geochemistry, Geophysics, Geosystems*, 12. https://doi.org/10.1029/2011gc003665

Thomas, C., Garnero, E.J., Lay, T., 2004. High-resolution imaging of lowermost mantle structure under the Cocos plate. *Journal of Geophysical Research-Solid Earth*, 109. https://doi.org/10.1029/2004jb003013

Thorne, M.S., Leng, K.D., Pachhai, S., Rost, S., Wicks, J., Nissen-Meyer, T., 2021. The Most Parsimonious Ultralow-Velocity Zone Distribution From Highly Anomalous SPdKS Waveforms. *Geochemistry, Geophysics, Geosystems*, 22. https://doi.org/10.1029/2020GC009467

Torsvik, T.H., Burke, K., Steinberger, B., Webb, S.J., Ashwal, L.D., 2010. Diamonds sampled by plumes from the core-mantle boundary. *Nature*, 466, 352-355. https://doi.org/10.1038/nature09216

Torsvik, T.H., Smethurst, M.A., Burke, K., Steinberger, B., 2008. Long term stability in deep mantle structure: Evidence from the similar to 300 Ma Skagerrak-Centered Large Igneous Province (the SCLIP). *Earth and Planetary Science Letters*, 267, 444-452. https://doi.org/10.1016/j.epsl.2007.12.004

Wang, Y., Wen, L.X., 2004. Mapping the geometry and geographic distribution of a very low velocity province at the base of the Earth's mantle. *Journal of Geophysical Research-Solid Earth*, 109. https://doi.org/10.1029/2003jb002674

Wang, Y., Wen, L.X., 2007. Geometry and P and S velocity structure of the "African Anomaly". *Journal of Geophysical Research-Solid Earth*, 112. https://doi.org/10.1029/2006jb004483

Wen, L.X., 2001. Seismic evidence for a rapidly varying compositional anomaly at the base of the Earth's mantle beneath the Indian Ocean. *Earth and Planetary Science Letters*, 194, 83-95. https://doi.org/10.1016/S0012-821x(01)00550-7

Zhao, C.P., Garnero, E.J., Li, M.M., McNamara, A., Yu, S.L., 2017. Intermittent and lateral varying ULVZ structure at the northeastern margin of the Pacific LLSVP. *Journal of Geophysical Research-Solid Earth*, 122, 1198-1220. https://doi.org/10.1002/2016jb013449

Zheng, X.F., Ouyang, B., Zhang, D.N., Yao, Z.X., Liang, J.H., Zheng, J., 2009. Technical system construction of Data Backup Centre for China Seismograph Network and the data support to researches on the Wenchuan earthquake. Chinese Journal of Geophysics, 52, 1412-1417. https://doi.org/10.3969/j.issn.0001-5733.2009.05.031

788 **Table 1.** All events used in this study. Events A-C (shown in red) are modeled in detail.

Date	Lat/Lon (°)	Depth (km)	Mw	φ/δ/λ (°)	Location
2019/04/23 (Event A)	24.71S/178.78W	384.18	6.0	3/84/-81	South of Fiji Islands
2019/03/20 (Event B)	15.58S/167.48E	129.68	6.3	184/61/95	Vanuatu Islands
2019/03/10 (Event C)	17.81S/178.61W	580.73	6.2	32/37/-157	Fiji Islands
2005/10/15	25.29N/123.43E	194.57	6.4	325/22/178	Taiwan
2011/09/03	20.79S/169.72E	151.62	7.0	19/32/161	Vanuatu Islands
2011/11/08	27.13N/125.77E	230.60	6.9	7/57/-68	Taiwan
2012/12/07	38.31S/176.08E	165.12	6.3	179/28/21	New Zealand
2013/03/24	20.76S/173.45E	14.42	6.0	126/89/-162	Vanuatu Islands
2013/06/15	33.82S/179.63E	200.45	6.0	232/27/133	Kermadec Islands
2013/08/28	27.73S/179.84E	429.01	6.2	192/65/15	Kermadec Islands
2014/03/02	27.34N/127.46E	124.88	6.5	6/68/-40	Ryukyu, Japan
2014/05/01	21.52S/170.12E	119.51	6.6	3/37/179	Loyalty Islands
2014/07/19	15.64S/174.18W	233.80	6.2	246/12/163	Tonga Islands
2014/12/10	25.51N/122.40E	262.02	6.1	89/72/-95	Taiwan
2016/08/04	24.98N/141.91E	522.70	6.3	358/80/-66	Volcano, Japan
2017/08/11	14.03N/120.65E	180.41	6.2	294/42/88	Luzon, Philippines
2018/04/02	24.73S/176.75W	93.18	6.1	351/71/-54	South of Fiji Islands
2018/09/06	18.24S/179.86E	686.61	7.9	305/60/15	Fiji Islands
2018/09/10	31.92S/179.16W	117.32	6.9	47/84/-50	Kermadec Islands
2018/09/16	25.26S/178.37E	590.96	6.5	252/38/-164	South of Fiji Islands
2018/10/30	39.07S/174.94E	225.84	6.1	168/43/33	New Zealand
2019/01/26	21.04S/179.01W	601.50	6.2	273/16/-64	Fiji Islands
2019/05/30	21.77S/176.13W	180.03	6.0	278/9/-11	Fiji Islands
2019/06/04	29.08N/139.17E	438.98	6.3	347/88/-75	Honshu, Japan
2019/07/27	33.16N/137.13E	376.63	6.3	157/79/59	Honshu, Japan
2019/07/31	16.28S/167.85E	187.81	6.6	290/67/27	Vanuatu Islands
2019/08/24	14.32S/167.07E	127.16	6.0	261/82/90	Vanuatu Islands
2019/10/21	19.07S/169.31E	245.04	6.4	177/59/65	Vanuatu Islands
2019/11/08	21.94S/179.42W	599.20	6.5	15/88/-77	Fiji Islands
2020/06/04	2.98N/128.15E	121.35	6.4	15/67/132	Indonesia
2020/06/13	28.80N/128.39E	171.48	6.6	1/70/-58	Ryukyu, Japan
2020/07/18	15.29S/172.82W	15.98	6.1	13/52/125	Samoa Islands

789

790

Table 2. Pearson's R-values between the observed S/ScS travel time residuals ($\delta t_S/\delta t_{ScS}$) and differential travel time residuals between S and ScS (δt_{ScS-S}) after corrections for different tomographic models: GyPSuM (Simmons et al., 2010), S40RTS (Ritsema et al., 2011), SEMUCB-WM1 (French and Romanowicz, 2015), TX2019slab (Lu et al., 2019), GLAD-M25 (Lei et al., 2020), SAW24B16 (Megnin and Romanowicz, 2000).

Tomographic models	$\delta t_S/\delta t_{ScS-S}$	$\delta t_{ScS}/\delta t_{ScS-S}$
GyPSuM	-0.11	0.51
S40RTS	-0.18	0.30
SEMUCB-WM1	-0.14	0.32
TX2019slab	-0.31	0.24
GLAD-M25	-0.29	0.42
SAW24B16	-0.24	0.28

Figure 1. Map showing locations of events (stars) and stations (triangles). Colored lines show the S-wave western edge of the Pacific LLVP determined by δV_S = 0 from different S-wave tomographic models: GyPSuM (Simmons et al., 2010), GLAD-M25 (Lei et al., 2020), S40RTS (Ritsema et al., 2011), SEMUCB-WM1 (French and Romanowicz, 2015). The ScS bounce points at the CMB with epicentral distance smaller than 85° are shown with pink dots. The yellow dashed line shows the representative great circle path from Tonga-Fiji to China. Events A-C modeled in detail are marked with red stars. The black box indicates the enlarged view in Figure 3.

Figure 2. Relationship between travel time residuals of S (δt_S) and ScS (δt_{ScS}) and differential travel time residuals between S and ScS (δt_{ScS-S}). (a-b) Results after correction for PREM (Dziewonski and Anderson, 1981). (c-d) Results after correction for GyPSuM (Simmons et al., 2010) at a depth of 0-2600 km. Pearson's R-values shown on the top-left corner in each panel quantify the correlations.

Figure 3. Observed δt_{ScS-S} and ScS/S amplitude ratio ($A_{ScS/S}$) projected at the ScS bouncing points at the CMB. δt_{ScS-S} are relative to (a) PREM (Dziewonski and Anderson, 1981) and (b) GyPSuM (Simmons et al., 2010). $A_{ScS/S}$ are for (c) original and (d) after correction for radiation patterns. The red dashed line shows the S-wave LLVP boundary from He and Wen (2012). The black dashed lines show the distances and azimuths taken from event A. The red and blue polygons in (b) show the extended LLVP region (LLVP limb) and high-velocity D″ layers, respectively, outlined by the measured δt_{ScS-S}. Note the number of points of the $A_{ScS/S}$ are less than those of the δt_{ScS-S} due to the discard of traces with ray paths of S or ScS near the nodal plane.

Figure 4. 2D S-wave velocity model for two adjacent azimuths: 300°-305° (profile I) and 305°-310° (profile II). (a-b) Cross-sections from Tonga-Fiji to China on profile I and profile II through the S-wave tomographic model GyPSuM (Simmons et al., 2010). Representative ray paths of S (solid) and ScS (dashed) with distances of event A (black lines) and event B (purple lines) which are nearly located at the same arc plane along the great circle path are shown, taking event A as 0°. Distance between event A and event B is ~ 16°. Locations of event A and event B are not displayed to better show the structures in the lowermost mantle. δV_S in the LLVP region in the GyPSuM are enhanced by 1.5 times. The red box in (a) indicates the LLVP limb. The blue box in (b) indicates the high-velocity D″ layer with δV_S discontinuity, and no further constraints about D″ layer structures is shown with dashed line. (c) Enlarged view of the black box in inset showing ScS bouncing points at the CMB of event A (black) and event B (purple) on profile I and profile II. The red dashed line shows the S-wave LLVP boundary from He and Wen (2012). The black dashed lines show the distances and azimuths taken from event A.

Figure 5. Comparison between stacked data (black) and 2D synthetics (red) of event A and event B on profile I (Az: 300°-305°, top panel) and profile II (Az: 305°-310°, bottom panel). Synthetics in left panel in each subfigure are for GyPSuM (Simmons et al., 2010) while in right panel are for the hybrid model in Figure 4a-b. Waveforms are aligned on S. The black dashed lines in each panel show the S and ScS arrival times predicted by PREM (Dziewonski and Anderson, 1981). The misfit functions (CC, σ_{L1}, σ_{L2}) for the LLVP limb between the data and synthetics are

calculated in the time window indicated by grey shaded region. The blue dashed line shows Scd arrivals generated from the high-velocity D″ layer. The green dashed line in (a) and (c) shows SKS arrivals on tangential components due to the anisotropy, after comparison with those on radial components (Figure S2). The blue dashed box in (d) shows the enlarged view in Figure 6.

Figure 6. Comparison between the data (black) and 2D synthetics (red) at the distance of 88°-96° of event B on profile II (Az: 305°-310°). Synthetics are for GyPSuM (Simmons et al., 2010) (left panel) and the hybrid model (right panel) in Figure 4b. Waveforms are aligned on S. The depth phase sS are followed by S. Anomalous Scd+S waveforms generated from high-velocity D″ layer are indicated by red arrows. The misfit functions (CC, σ_{L1}, σ_{L2}) for the high-velocity D″ layer between the data and synthetics are calculated in the time window indicated by grey shaded region.

Figure 7. Trade-offs between δV_S and H for the LLVP limb on profile I (Az: 300°-305°). Misfit functions are CC (left), σ_{L1} (middle), and σ_{L2} (right) for event A in Figure 5a, respectively. The best fitting model (δV_S = -4%, H = 30 km) with highest CC (lowest σ_{L1} and σ_{L2}) is shown with red star. Models with constant value of product of δV_S and H (-1.2 km, -2.4 km, -3.6 km) are shown with black dashed lines.

Figure 8. Trade-offs between δV_S and H for the high-velocity D″ layer on profile II (Az: 305°-310°). (a) Schematic diagram of the high-velocity D″ layer described by δV_S jump at the discontinuity and H of the D″ layer. (b) Misfit functions are CC, σ_{L1}, and σ_{L2} for event B in Figure 6. The best fitting model (δV_S = +2.2%, H = 320 km) with highest CC (lowest σ_{L1} and σ_{L2}) is shown with red star.

Figure 9. Comparison between the stacked data (black) and 3D synthetics (red) of event A on (a) profile I (Az: 300°-305°) and (b) profile II (Az: 305°-310°). Synthetics are for GyPSuM (Simmons et al., 2010) and 3D hybrid model shown in Figure 3b. Waveforms are aligned on S. The black dashed lines in each panel show the S and ScS arrival times predicted by PREM (Dziewonski and Anderson, 1981). The blue dashed lines show Scd arrivals generated from the high-velocity D″ layer.

Figure 10. Comparison between the data (black) and 3D synthetics (red) at the distance of 90°-92° on azimuth profiles of event A. Synthetics are for (a) GyPSuM (Simmons et al., 2010) and (b) 3D hybrid model shown in Figure 3b. Waveforms are aligned on S. Note the delayed ScS arrivals at the azimuth smaller than 305° and becomes normal at the azimuth larger than 305°, showing strong lateral 3D structural variation. Anomalous delayed ScS waveforms generated from the LLVP limb are indicated by yellow patch.

Figure 11. Comparison between the data (black) and 3D synthetics (red) at the distance of 88°-95° on profile II (a) and on azimuth profile at the distance of 90°-95° (b) of event B. Azimuth in (b) is taken from event B. Synthetics are for GyPSuM (Simmons et al., 2010) and 3D hybrid

882 model in Figure 3b. Waveforms are aligned on S. The depth phase sS are followed by S.
883 Anomalous Scd+S waveforms generated from the high-velocity D″ layer are indicated by yellow
884 patches. Note the normal waveforms at the azimuth smaller than 310° and anomalous Scd+S
885 waveforms at the azimuth larger than 310°, showing strong lateral 3D structural variation.
886
887 **Figure 12**. Cartoons showing different morphology at the western edge of the Pacific LLVP. (a)
888 On profile I, LLVP has a limb with a low height in the case of the absence of the slab. (b) On
889 profile II, LLVP has a dome-like structure due to the slab pushing.
890

Figure 1.

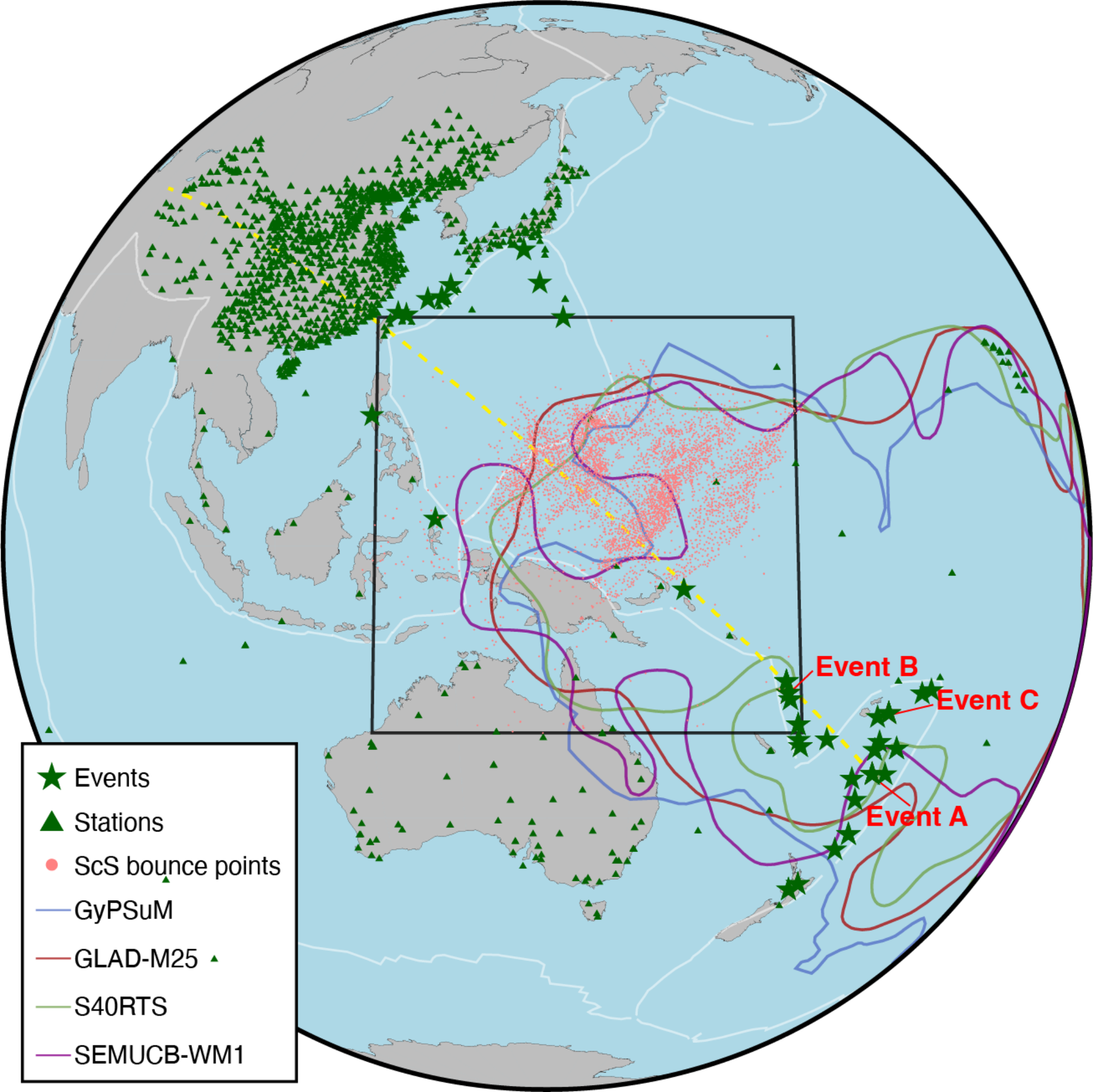
Event B
Event C
Event A
Events
Stations
ScS bounce points
GyPSuM
GLAD-M25
S40RTS
SEMUCB-WM1

Figure 2.

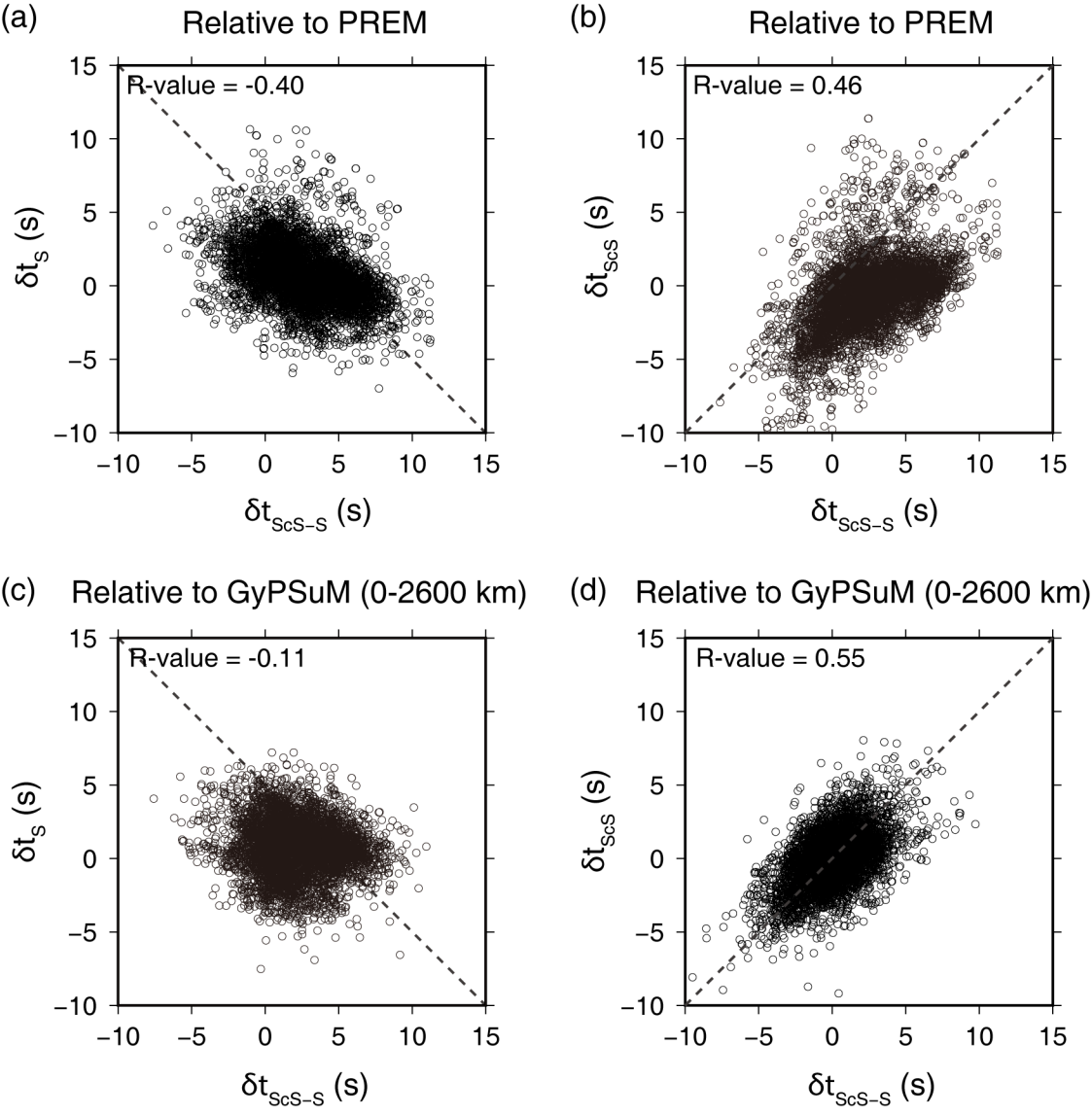
(a)
Relative to PREM
R-value = -0.40
δt_S (s)
δt_ScS−S (s)
(b)
Relative to PREM
R-value = 0.46
δt_ScS (s)
δt_ScS−S (s)
(c)
Relative to GyPSuM (0-2600 km)
R-value = -0.11
δt_S (s)
δt_ScS−S (s)
(d)
Relative to GyPSuM (0-2600 km)
R-value = 0.55
δt_ScS (s)
δt_ScS−S (s)

Figure 3.

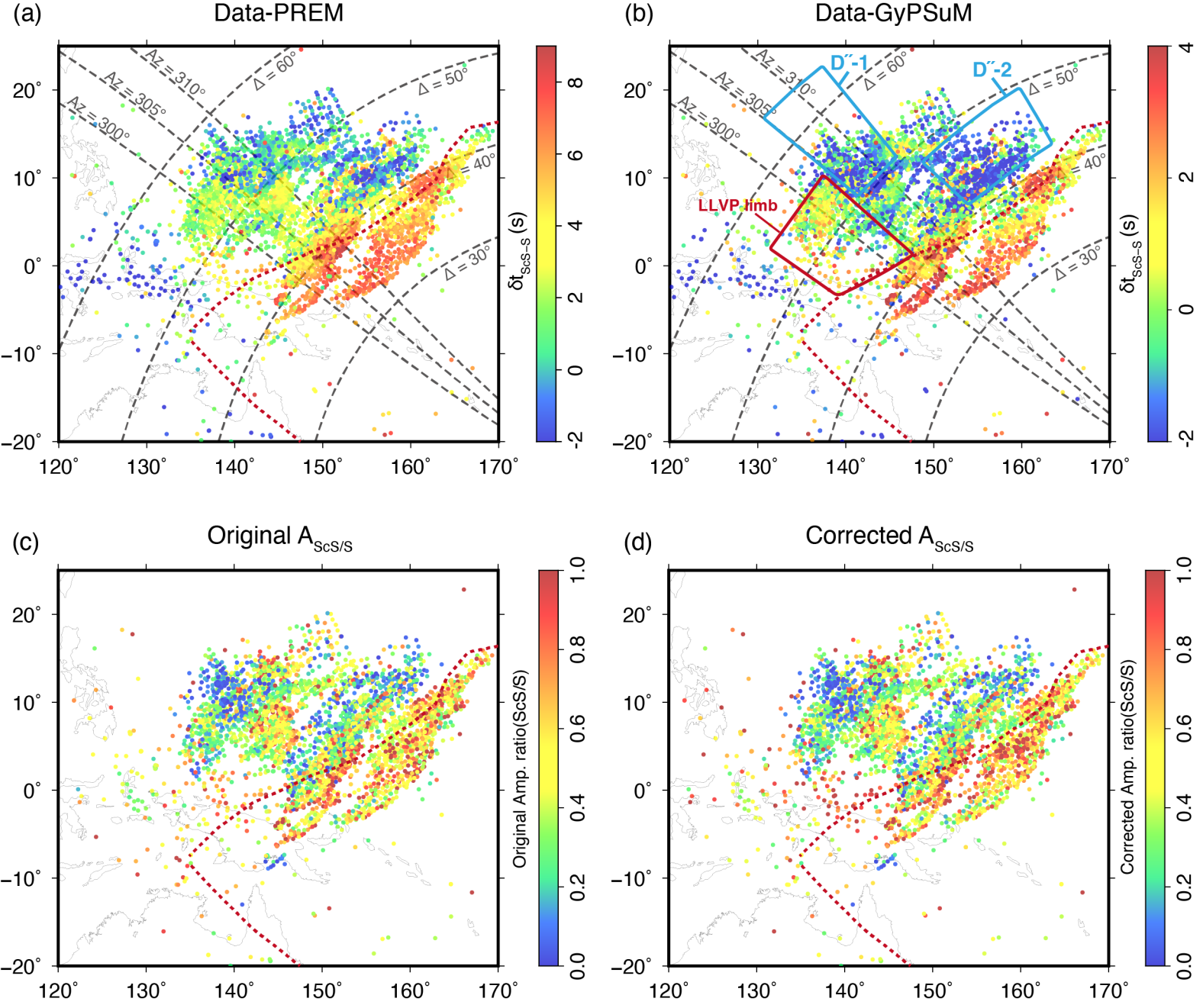
(a)
Data-PREM
(b)
Data-GyPSuM
(c)
Original A$_{ScS/S}$
(d)
Corrected A$_{ScS/S}$
Az = 300°
Az = 305°
Az = 310°
Δ = 60°
Δ = 50°
Δ = 40°
Δ = 30°
D″-1
D″-2
LLVP limb
δt$_{ScS-S}$ (s)
Original Amp. ratio(ScS/S)
Corrected Amp. ratio(ScS/S)
120°
130°
140°
150°
160°
170°
20°
10°
0°
−10°
−20°

Figure 4.

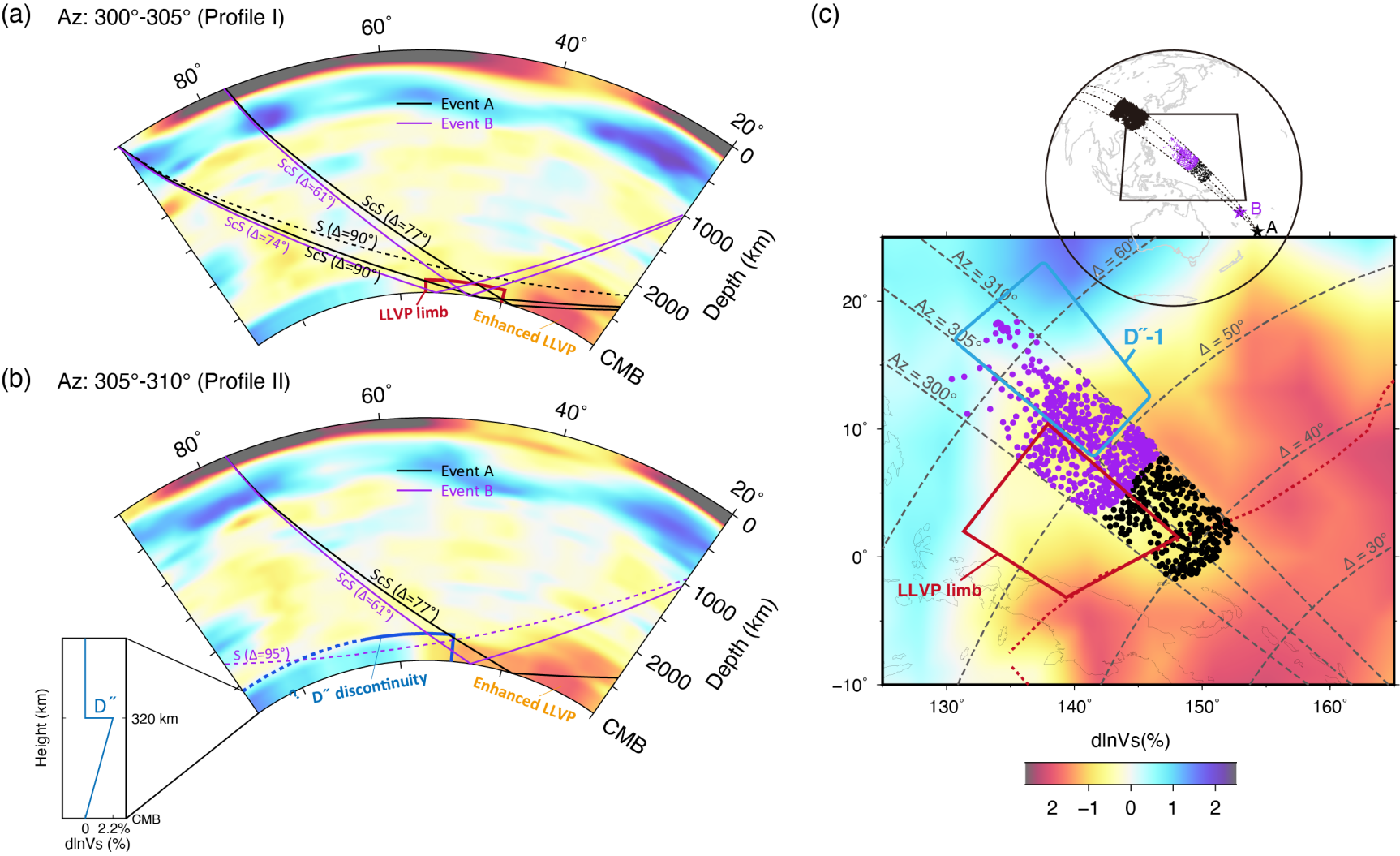
(a)
Az: 300°-305° (Profile I)
60°
40°
80°
20°
0
1000
2000
Depth (km)
CMB
Event A
Event B
ScS (Δ=61°)
ScS (Δ=77°)
ScS (Δ=74°)
S (Δ=90°)
ScS (Δ=90°)
LLVP limb
Enhanced LLVP
(b)
Az: 305°-310° (Profile II)
60°
40°
80°
20°
0
1000
2000
Depth (km)
CMB
Event A
Event B
ScS (Δ=61°)
ScS (Δ=77°)
S (Δ=95°)
D″ discontinuity
Enhanced LLVP
Height (km)
D″
320 km
CMB
0
2.2%
dlnVs (%)
(c)
B
A
Δ = 60°
Az = 310°
Az = 305°
Az = 300°
D″-1
Δ = 50°
Δ = 40°
Δ = 30°
LLVP limb
20°
10°
0°
−10°
130°
140°
150°
160°
dlnVs(%)
2
−1
0
1
2

Figure 5.

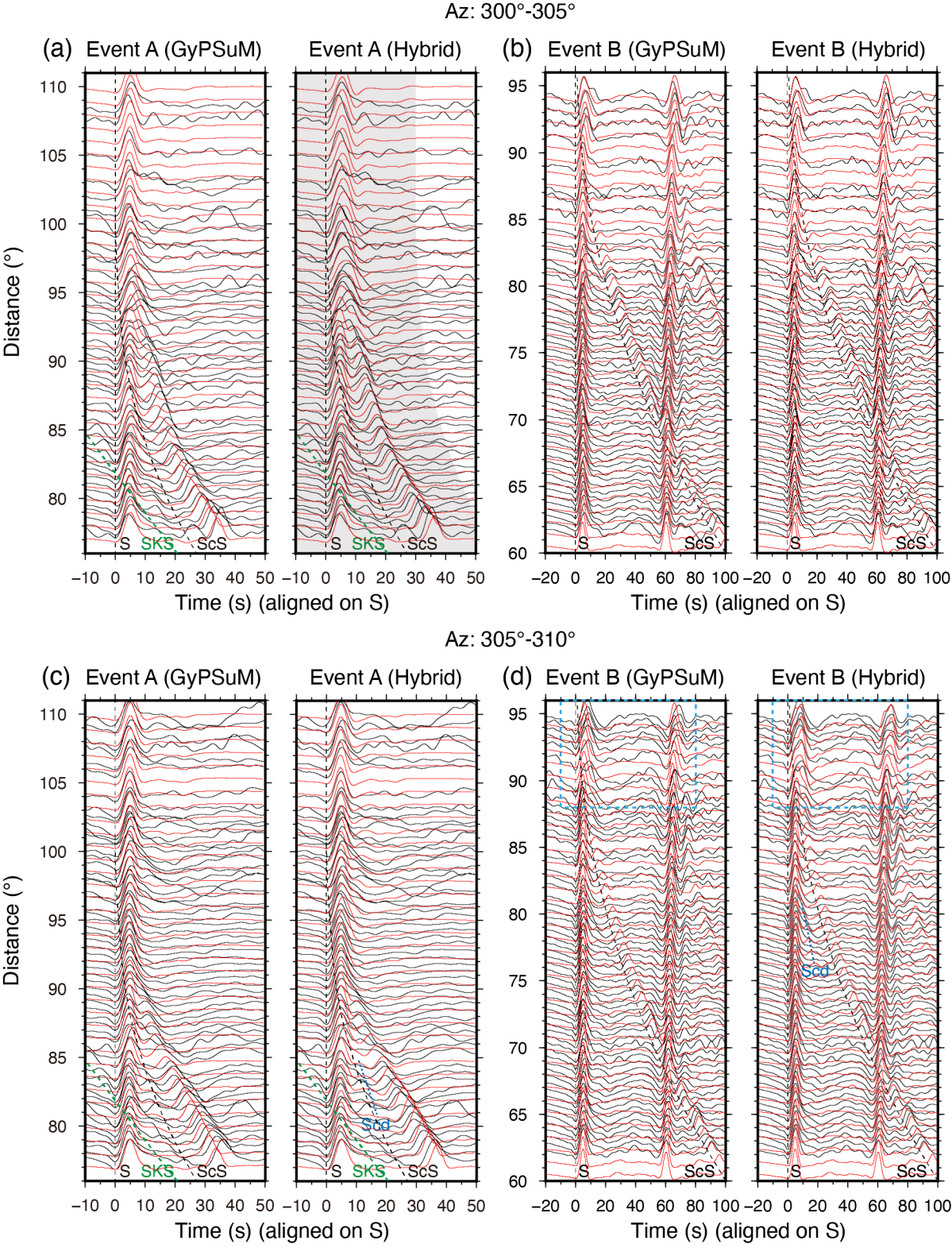
Az: 300°-305°
(a)
Event A (GyPSuM)
Event A (Hybrid)
(b)
Event B (GyPSuM)
Event B (Hybrid)
Distance (°)
Time (s) (aligned on S)
S
SKS
ScS
Az: 305°-310°
(c)
(d)
Scd

Figure 6.

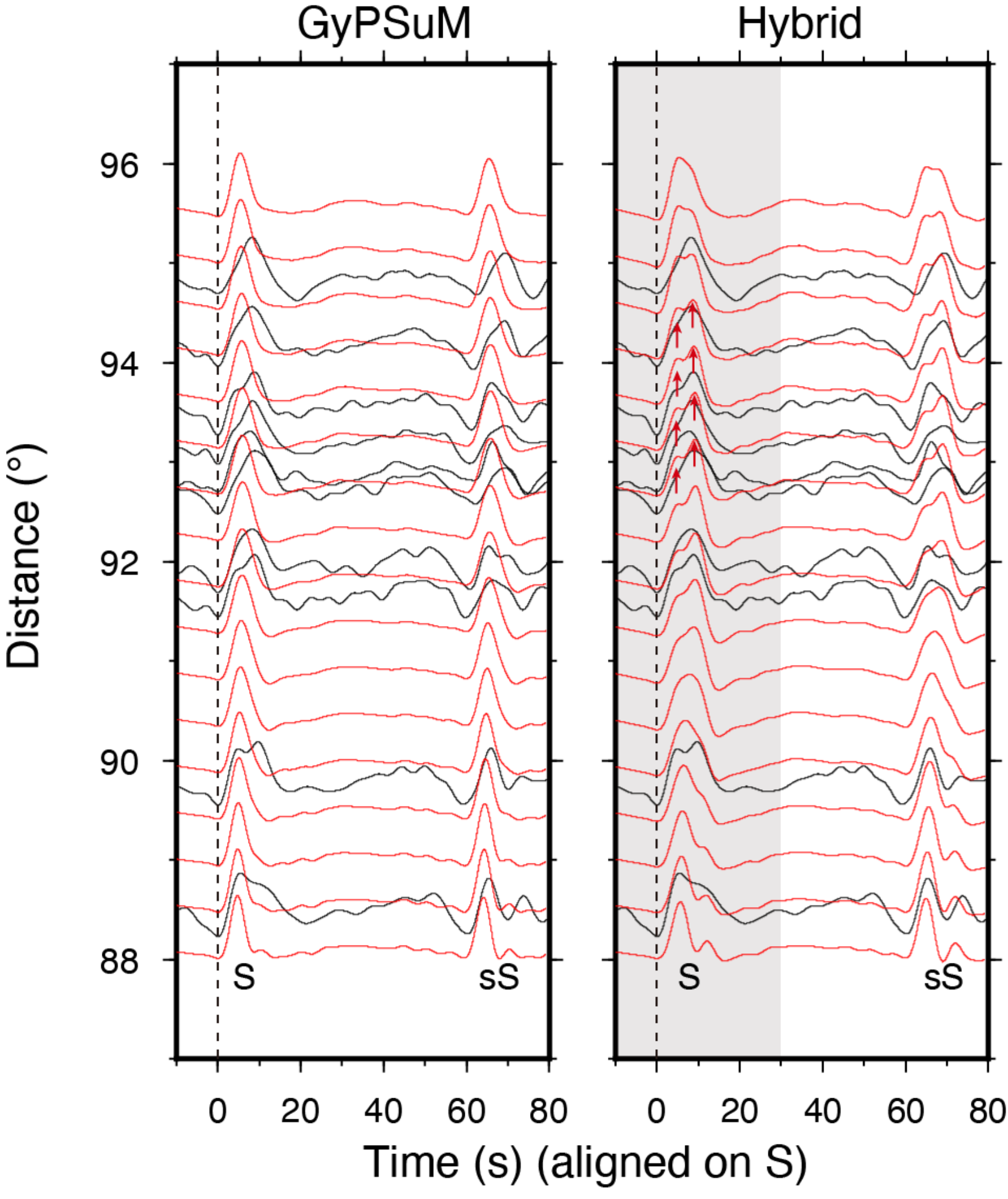
GyPSuM
Hybrid
96
94
92
90
88
Distance (°)
S
sS
S
sS
0
20
40
60
80
0
20
40
60
80
Time (s) (aligned on S)

Figure 7.

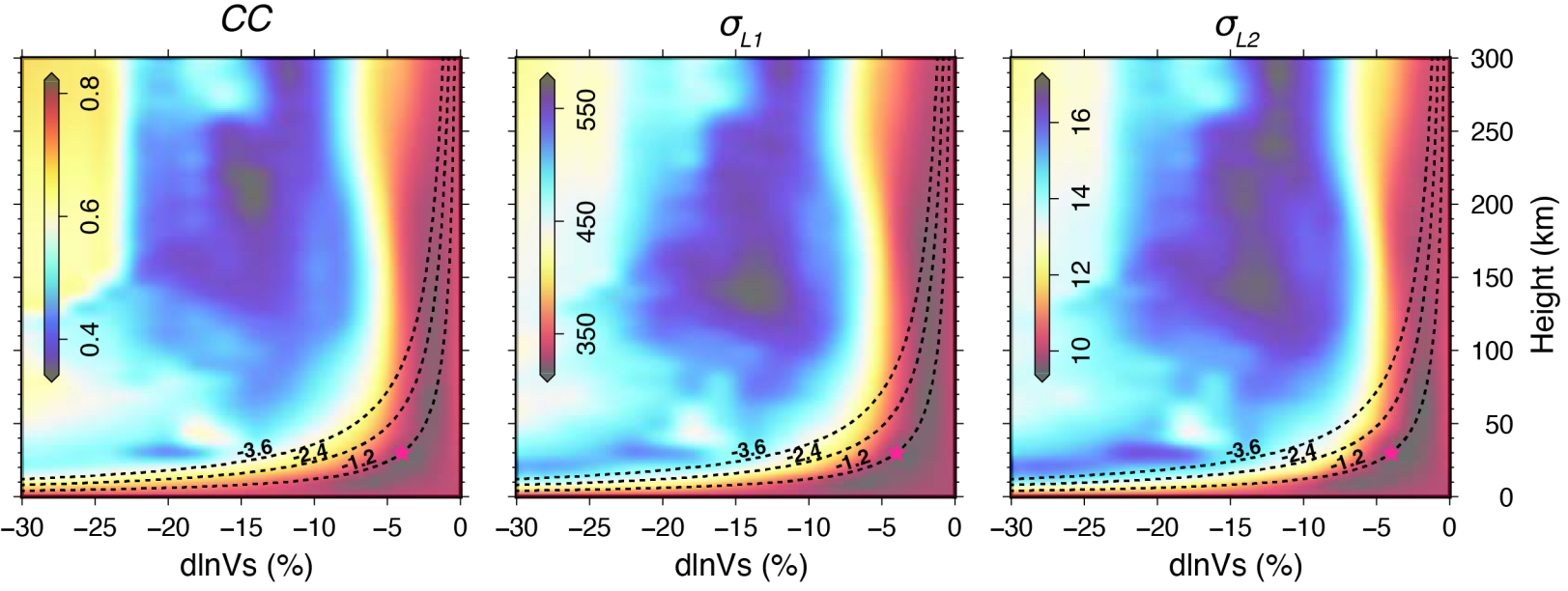
CC
0.8
0.6
0.4
σ_{L1}
550
450
350
σ_{L2}
16
14
12
10
-3.6
-2.4
-1.2
−30 −25 −20 −15 −10 −5 0
dlnVs (%)
300 250 200 150 100 50 0
Height (km)

Figure 8.

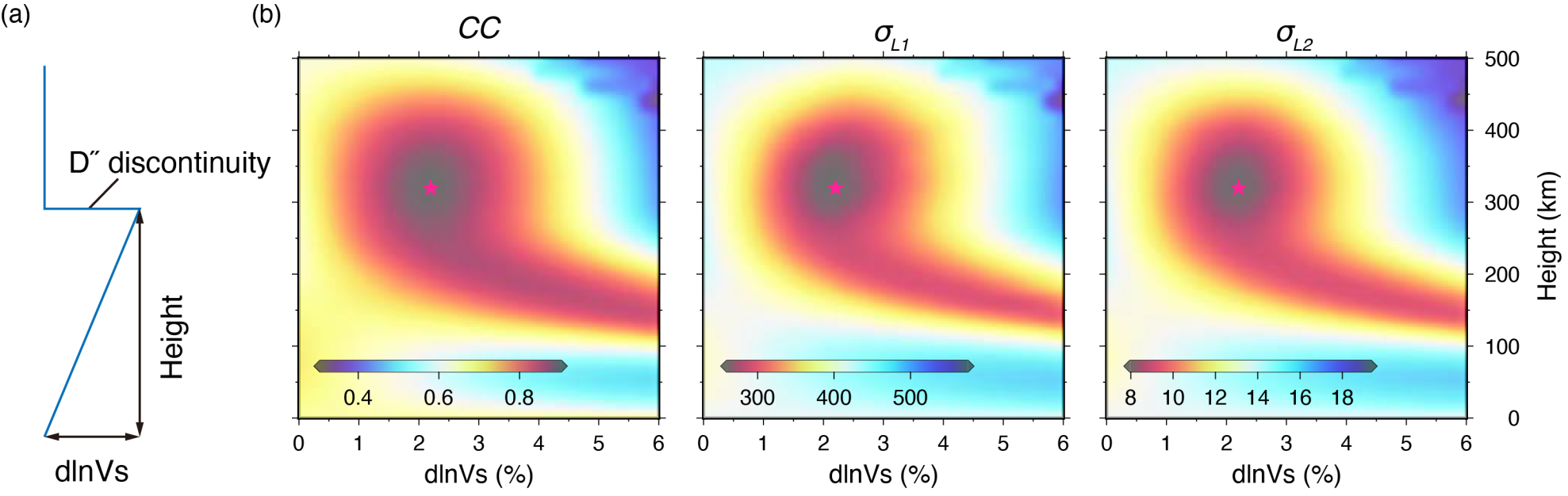
(a)
D″ discontinuity
Height
dlnVs
(b)
CC
σ_{L1}
σ_{L2}
0.4 0.6 0.8
300 400 500
8 10 12 14 16 18
0 1 2 3 4 5 6
dlnVs (%)
500 400 300 200 100 0
Height (km)

Figure 9.

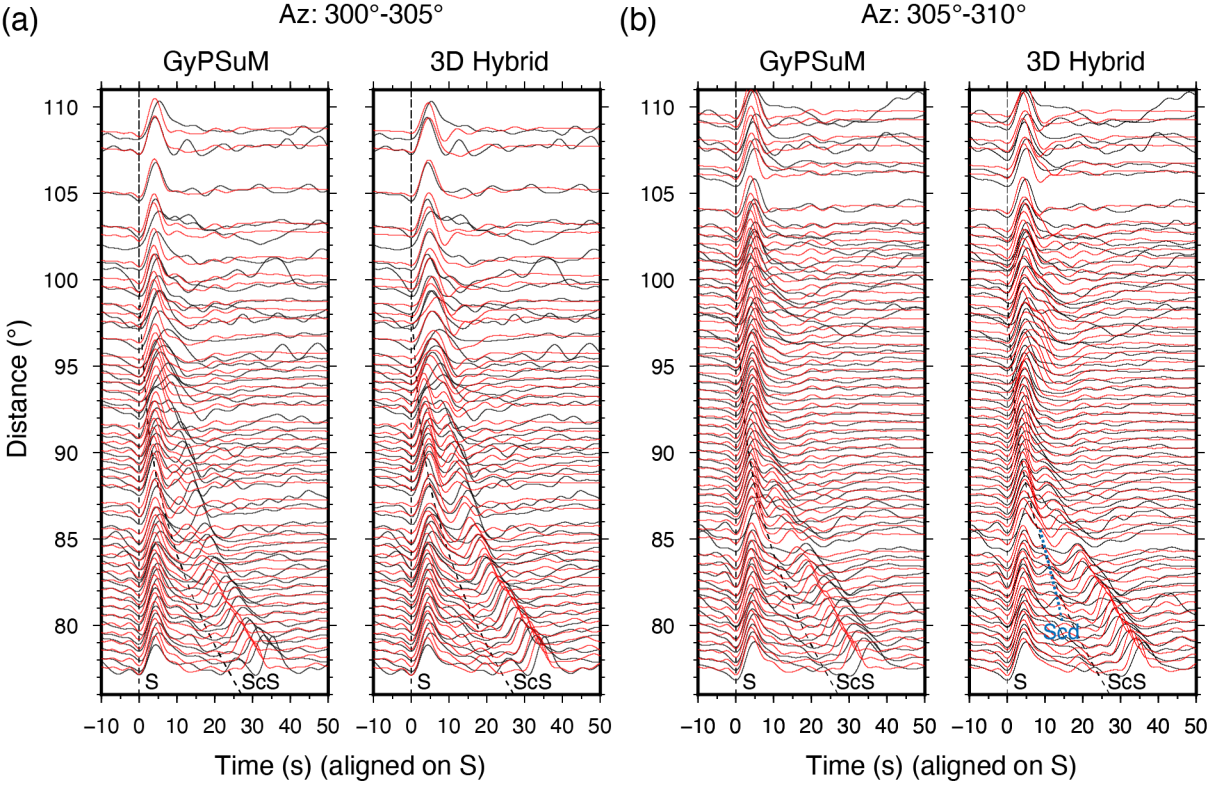
(a)
Az: 300°-305°
GyPSuM
3D Hybrid
(b)
Az: 305°-310°
GyPSuM
3D Hybrid
Distance (°)
110
105
100
95
90
85
80
S
ScS
Scd
−10 0 10 20 30 40 50
Time (s) (aligned on S)

Figure 10.

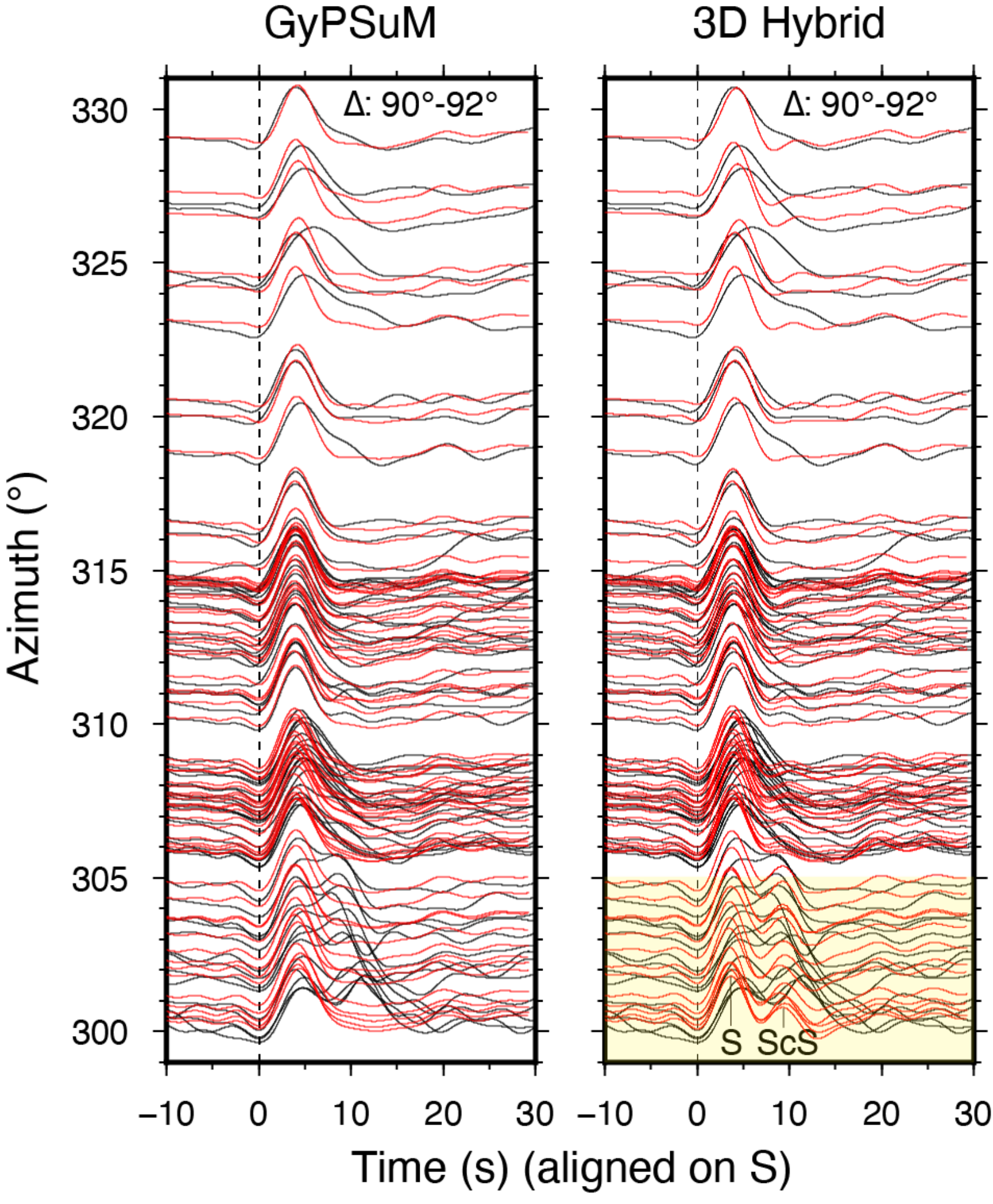
GyPSuM
3D Hybrid
Δ: 90°-92°
Δ: 90°-92°
330
325
320
315
310
305
300
Azimuth (°)
S
ScS
−10
0
10
20
30
−10
0
10
20
30
Time (s) (aligned on S)

Figure 11.

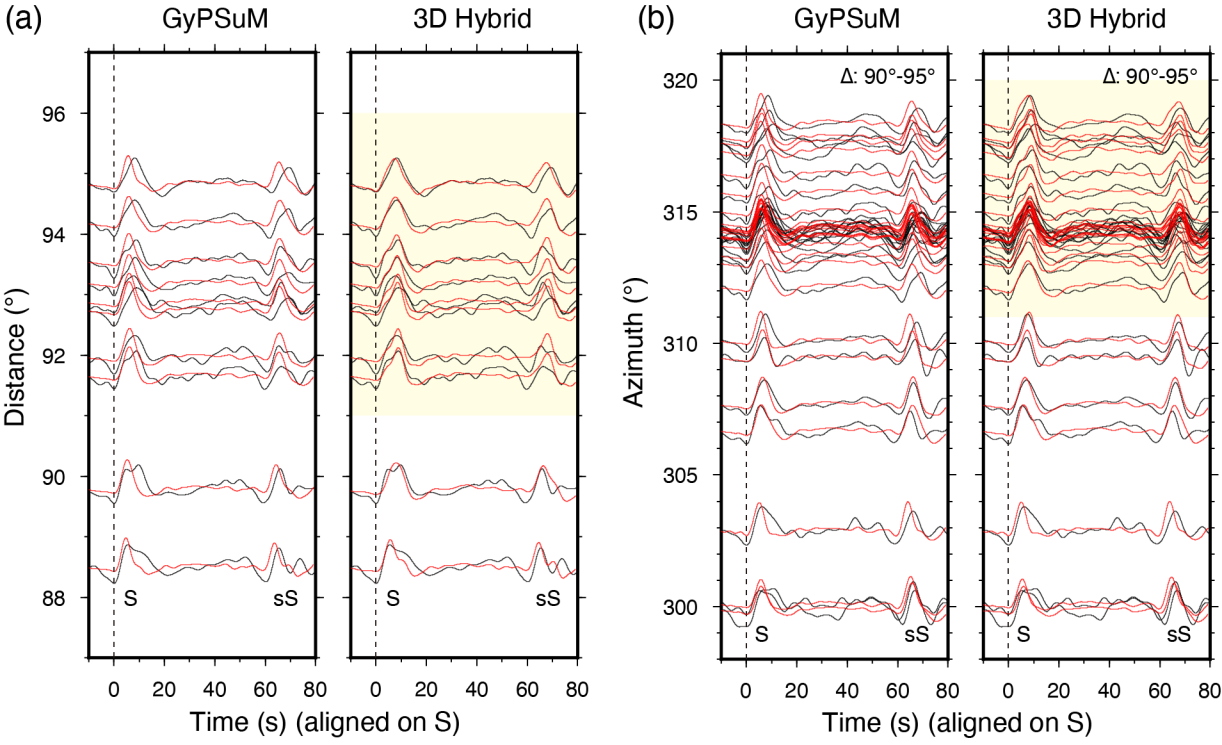
(a)
GyPSuM
3D Hybrid
Distance (°)
96
94
92
90
88
S
sS
0
20
40
60
80
Time (s) (aligned on S)
(b)
GyPSuM
3D Hybrid
Δ: 90°-95°
Azimuth (°)
320
315
310
305
300
S
sS
Time (s) (aligned on S)

Figure 12.

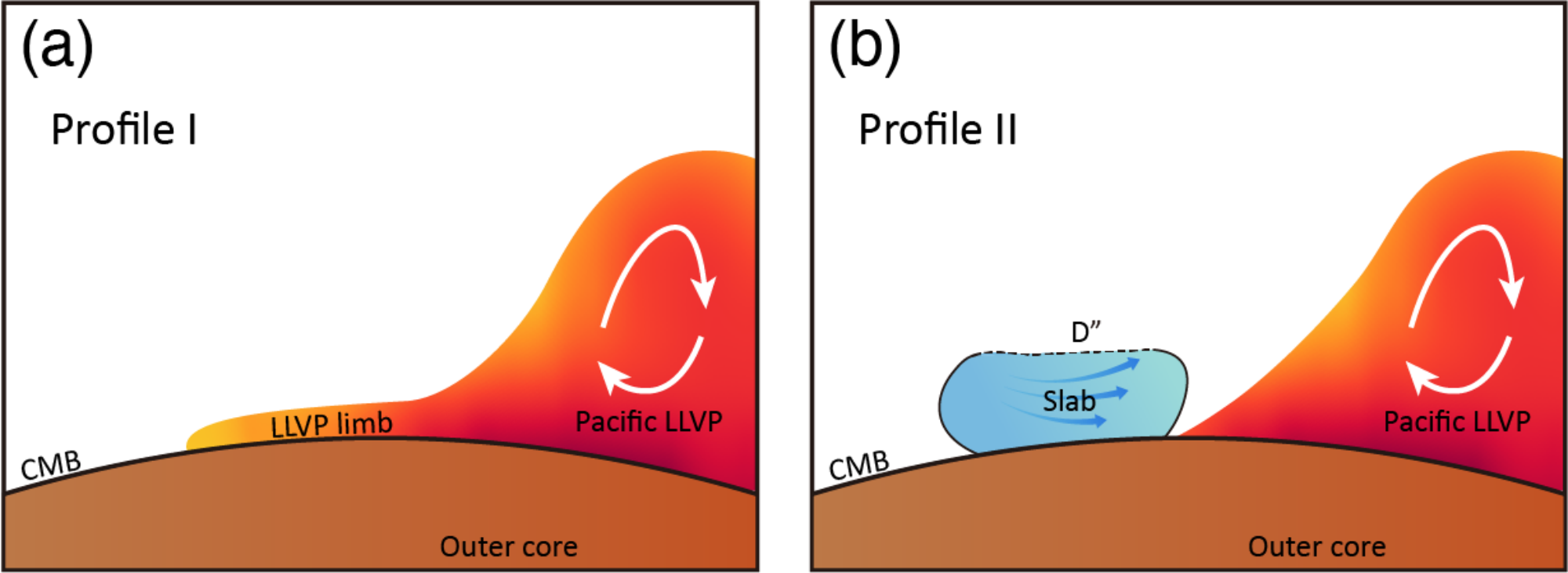
(a)
Profile I
LLVP limb
Pacific LLVP
CMB
Outer core
(b)
Profile II
D”
Slab
Pacific LLVP
CMB
Outer core